HIGH PRESSURE THERMAL TRIAXIAL COMPRESSION OF MANCOS SHALE

by

ANDREA TYRRELL

B.S., University of Florida, 2020

A thesis submitted to the

Faculty of the Graduate School of the

University of Colorado in partial fulfillment

of the requirement for the degree of

Master of Science

Department of Civil, Environmental and Architectural Engineering

2022

Committee Members:

Yida Zhang, Chair

Richard A. Regueiro

Yunping Xi

Tyrrell, Andrea (M.S., Civil Engineering, Department of Civil, Environmental and Architectural Engineering)
High Pressure Thermal Triaxial Compression of Mancos Shale

Thesis directed by Professor Yida Zhang

ABSTRACT

Conventional triaxial tests on materials have been modified to apply complex loading paths, large confining pressures, and elevated temperatures on specimens. These tests offer insights into how materials behave under various mechanical and environmental conditions. The experimental results obtained can be used to calibrate and validate existing numerical and analytical models in solving engineering problems across distinct length and time scales which cannot be accomplished within the laboratory.

This thesis focuses on the development of the MTS-815 High Pressure Triaxial testing device at the University of Colorado Boulder (CUBoulder) and the usage of the derived data in advancing our understanding of the thermomechanical behavior of frictional materials. The first part of this thesis details the basic components and the developed procedures for performing high-pressure triaxial tests. Preliminary test results helped to understand the mechanics of the machine and how reliable results should be obtained. The second part of this thesis utilizes the procedures developed to investigate the thermomechanical behavior of Mancos Shale. The purpose of this study was to prepare the testing device for conducting thermomechanical tests on plastic-bonded granular materials as part of CUBoulder's PSAAP center effort. The preliminary results on Mancos shale also helps us understand the potential of shale as host rock for deep geologic disposal of high-level radioactive wastes. The shale triaxial data was finally interpreted by a directional damage theory. A supplementary study of how damage levels affect the permeability of Mancos Shale was also performed.

ACKNOWLEDGEMENTS

I would like to express my sincere gratitude to my advisor, Dr. Yida Zhang, for his unconditional support throughout my M.S. studies and research at the University of Colorado Boulder. He continuously motivated me throughout my graduate experience by offering valuable insights, reassurance, and endless guidance. I would like to extend my gratitude to Dr. Richard A. Regueiro and Dr. Yunping Xi for serving as my committee members.

I sincerely thank the faculty and staff within the Department of Civil, Environmental and Architectural Engineering for providing me with the opportunity to advance my education. With their help and guidance, I feel well equipped to enter the industry as a geotechnical engineer.

I sincerely appreciate the love and support of my friends and family throughout my experience. They continuously cheered me on and supported me through all my decisions. I would also like to extend my gratitude to Dr. Yao Wang and Dr. Mitul Sisodiya who assisted me with various trainings. They provided me great advise which significantly contributed to my success.

I greatly appreciate the opportunity to work under the Predictive Science Academic Alliance Program (PSAAP) III Centers funded by the National Nuclear Security Administration. I recognize that this work would not be possible without the center's financial support. I am also grateful for the opportunity provided by the center to intern at Sandia National Laboratories.

TABLE OF CONTENTS

LIST OF FIGURES

LIST OF TABLES

CHAPTER 1: INTRODUCTION

1.1 Motivation

Triaxial testing is a versatile laboratory procedure commonly used to study the mechanical behavior of geomaterials. The test subjects materials to an axisymmetric triaxial state by surrounding the specimen with a fluid to apply confining pressure while simultaneously loading the specimen axially using an axial piston. Since its initial invention by von Kármán (1911), the triaxial device has been modified and updated to perform test at elevated temperatures, higher pore pressures, and larger confining pressures (Paterson and Wong, 2005). Through the addition of servo-controller equipment, more complex loading paths may be applied to samples. These modifications further broadened the ability to study the mechanical behavior of materials exposed to different environmental conditions. Furthermore, the application of triaxial testing has expanded beyond geomaterial experimentation to the mechanical testing of other porous and particulate materials.

The ultimate goal of the current project is to acquire thermal triaxial data to calibrate and validate numerical models for compressed mock High Explosive (HE) materials. Mock HE is a plastically bonded granular material that has some properties of epoxy resins (plasticity, creep, thermal softening) and can also exhibit frictional behaviors typical for granular materials (pressure-dependency, dilation, breakage) (Gratton et al., 2009). The overarching goal of this research is to understand and model the behaviors of explosive energetic materials during storage and transportation. Mock material with similar properties to the HE is often tested experimentally to eliminate the risk of ignition and supply data for the numerical models. Specifically, triaxial testing allows for mock HE materials to be subjected to quasi-static confined compression under complex

loading paths. While triaxial experimentation is one of the many methods for obtaining the mechanical data for mock HEs, they allow for testing specimens at sizes more representative of the actual HE.

The University of Colorado Boulder has recently acquired a high pressure thermal triaxial device with the capabilities of testing such materials. However, it was recently equipped with new electronics, controller, and pumping systems that were not systematically tested or verified. It became necessary to ensure the machine worked properly as designed for standard-sized specimens (2-inch diameter by 4-inch height), prior to applying the platform for probing the behaviors of mock Hes at smaller sample sizes (1-inch diameter by 2-inch height). To preserve mock HE samples, preliminary tests were performed on Mancos Shale specimens that were readily available in the laboratory. These tests helped develop operational procedures to reduce errors and pave the path for future testing on the more expensive mock HE specimens.

The use of Mancos Shale as a dummy testing material also has an added benefit in helping assess shale as a host rock for deep geologic disposal of high-level radioactive waste (HLW). Due to temperature, moisture, and stress state changes associated with the excavation of underground repositories and storage of heat generating wastes, the macroscopic properties of the host rock will be inevitably affected. Furthermore, the microstructure of the host rock evolves under such conditions leading to uncertainty in processes such as subcritical crack growth which effects the long-term performance of HLW isolation. High pressure thermal triaxial tests allow for the study of how such changes impact the macroscopic material properties. The data obtained experimentally can be used to calibrate existing models to further study microstructural processes and material performance across larger time and length scales.

1.2 Research Objectives

This thesis aims to study the thermo-mechanical behavior of Mancos Shale while documenting the laboratory procedures to improve the reliability of experimental results. The experimental work presented is intended to later guide the testing of virgin and recycled mock HE and other materials to support the work of the PSAAP Center for Micromorphic Multiphysics Porous and Particulate Materials Simulations with Exascale Computing Workflows at CUBoulder. The goals of this study are to: (1) troubleshoot the High Pressure Thermal Triaxial device at CUBoulder and develop testing methods for standard specimens; (2) apply these methods to investigate the effects of temperature and confining pressure on the thermo-hydro-mechanical properties of Mancos Shale; (3) model the stress-strain behavior of Mancos Shale using a recently developed directional damage theory. The objectives are discussed in further detail below.

1.2.1 Objective 3

Objective 1 is to troubleshoot and document the procedures used to improve the reliability of high pressure and elevated temperature triaxial tests. In addition, a recommended protocol for running standard thermal triaxial experiments are documented for its future application on mock HE specimens.

1.2.2 Objective 2

Objective 2 is to investigate the thermo-hydro-mechanical (THM) behavior of Mancos Shale. A series of thermal triaxial compression tests is conducted on the specimens to study their stress-strain curves under loading-unloading-reloading stress paths at different temperatures and confining pressures. A few permeability tests are also performed on post-test Mancos Shale

samples to investigate the change of transport properties due differing levels of damage. Possible improvements for future permeability tests are also suggested.

1.2.3 Objective 3

The final objective is to utilize an existing constitutive model to predict the stress-strain response of Mancos Shale. The data from the room-temperature compression tests is used to calibrate the directional damage model proposed by Sisodiya and Zhang (2021) using a MATLAB driver described in Sisodiya (2021). After calibration, the directional damage model is used to simulate tunnel excavation in a Mancos Shale formation in ABAQUS leveraging an existing user material subroutine (UMAT) code.

1.3 Thesis Arrangement

This thesis is organized into eight chapters. Chapter 1 discusses the motivation, main objectives, and arrangement of this thesis. Chapter 2 presents a literature review on deep geological disposal to support the importance of experimentally studying Mancos Shale. Previous studies on HE and mock HE are also discussed to support the planned experimental work in the near future. Chapter 3 introduces the device used for the experimental work and its limitations. Chapter 4 discusses the testing procedures developed and used for high pressure thermal triaxial experiments. The debugging processes and improvements made are also mentioned. Chapter 5 investigates the macroscopic responses of Mancos Shale from the triaxial experimental results. Chapter 6 then investigates the transport properties of damaged Mancos Shale through permeability tests. Some suggestions to improve these testing methods are also discussed. Chapter 7 outlines the calibration of the directional damage model based on the triaxial test results. This chapter also presents the implementation of the calibrated model in ABAQUS to simulate tunnel excavation within a Mancos Shale formation. Chapter 8 summarizes the main findings of this thesis.

CHAPTER 2: BACKGROUND

2.1 Deep Geologic Disposal

Deep geologic disposal of radioactive waste is a proposed method for storing and disposing of high-level radioactive waste (HLW). These wastes are typically byproducts of nuclear reactor operations which can negatively impact the environment and human life if not safely handled and permanently disposed of. Therefore, full life-cycle analyses which look at the generation, management, and disposal of HLW are typically required to ensure adequate levels of safety are met. Deep geologic disposal has gained increasing support from these assessments and involves disposing of HLW in repositories located in deep and stable rock formations (Berg and Brennecke 2013) in conjunction with an engineered barrier system (EBS) to optimize radionuclide containment (Kim et al. 2011). EBS components include canisters which contain the HLW, buffers surrounding the canisters, and backfill to stabilize the structure and further isolate the waste. Potential host rock candidates to contain these components salt, crystalline rocks (granite), or argillites (shale, claystone) formations (Berg and Brennecke 2013).

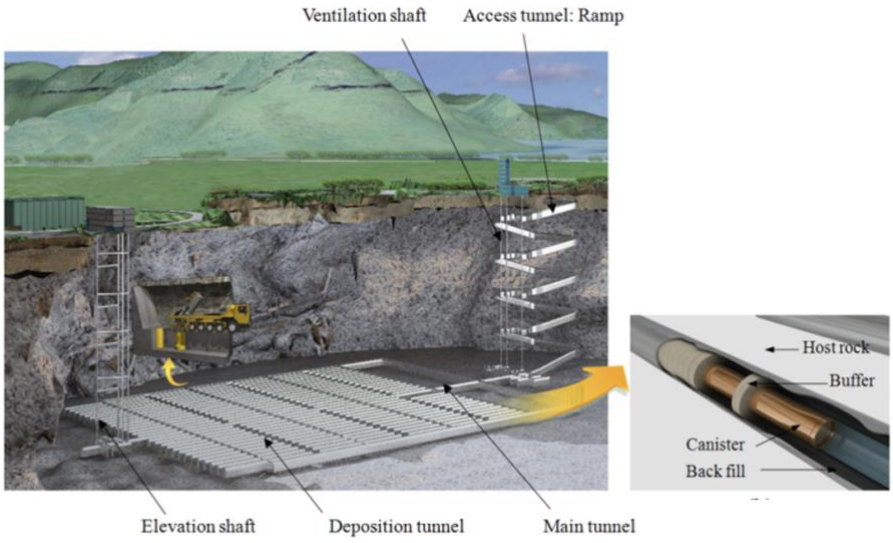

Figure 2.1: Repository schematic for HLW disposal (image from Kim et al. (2011))

Despite tremendous research efforts over the past decades, there remain uncertainties in the long-term performance of HLW repositories. The U.S. Nuclear Regulatory Commission requires a 1-million-year service life of HLW repositories. To meet this requirement, it is necessary to thoroughly understand the behaviors of the host rock and adequately simulate its long-term performance.

The long-term performance of repositories is dependent on existing damage, excavation, construction, and the heat generating nature of HLW. These factors affect the level of disturbance and damage present in the host rock mass which leads to challenges in selecting appropriate locations for HLW disposal (Zhang 2018). Excavation disturbed zones (EdZ) and excavation damage zones (EDZ) result from the changes in stress state that occur during these processes. Tsang et al. 2005 defined EdZ as zones subject to changes in hydromechanical and geo-mechanical properties while EDZ are zones subject to alterations in transport properties in addition to the changes observed in the EdZ. The EDZ is of most importance since transport properties, such as permeability, significantly affect the ability of repositories to isolate the radioactive material. Micro and macro-fracturing due to the redistribution of stresses in the host rock further affect the transport and mechanical properties of the rock and are influenced by time-dependent microscale processes such as subcritical crack growth, crack healing, and creep (Armand et al. 2014, Zhang 2018).

One viable host rock option for deep geological disposal is shale rock which contains clay minerals along with silicates and carbonates (Zhang 2018, Wang et al. 2021). The interest in this rock for repositories comes from beneficial properties such as its low hydraulic permeability, the ability to self-seal, a stable microstructure, and high sorption capacity of radionuclides (Huang et al. 1986, Sellin and Leupin 2013, Zhang 2018). These desired properties may experience changes overtime

after repository construction, thus influence shale's overall ability to protect the biosphere and human life (Grambow 2016). To assess the ultimate performance of shale rock for deep geologic disposal, it is necessary to understand the macroscopic and microscopic processes that contribute to the shale's thermal-hydrological-mechanical-chemical behaviors over large time spans.

Macroscopic studies utilize various laboratory procedures to characterize geo-mechanical properties of shale. Lora et al. (2016) studied the geo-mechanical properties of Marcellus Shale through monotonic and multi-stage triaxial tests to interpret the nonlinearity, pressure dependency, and anisotropic nature of shale. Several other studies also show that the Young's modulus measured parallel to the bedding plane is greater than that measured perpendicular to the bedding plane (Sayers 2013, Masri et al. 2014). Gao et al. (2015) additionally found that the anisotropic nature of shale results in more complex failure patterns and that the tensile strength parallel to the plane of bedding is significantly stronger than the direction perpendicular to the bedding plane. Other short-term triaxial tests have shown the dependence of elastic modulus on orientation and confining pressure (Islam and Skalle 2013, Lora et al. 2016, Zhang 2018).

Due to the heat generation of HLW additional studies have focused on the effect of elevated temperatures on the behavior of shale. It has been reported that the permeability, porosity, and fracture toughness of shale increase with increases in temperature (Kang et al. 2015, Chandler et al. 2017). Masri et al. (2014) additionally found that the Young's Modulus and compressive strength of Tournemire Shale decrease while the Poison's ratio increases with increasing temperature. These results are presented in the stress strain curve shown in Figure 2.2 and reflect the softening effect experienced by the material at elevated temperatures.

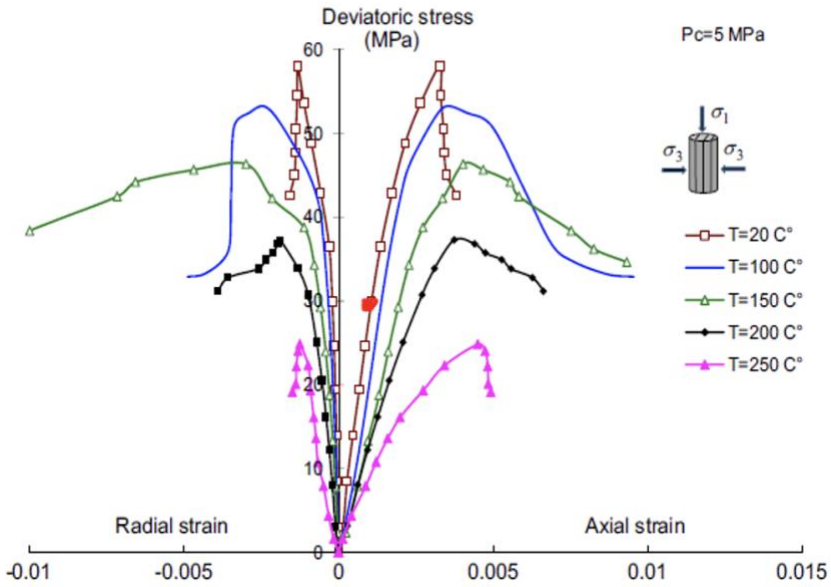

Figure 2.2: Triaxial compression of Tournemire shale results at elevated temperatures (image from Masri et al. (2014))

Transport and mechanical properties are critically affected by the microstructure of shale which will inevitably change due to stress redistributions during the excavation of repositories and variations in moisture and temperature due to the heat generating radioactive waste (Josh et al. 2012). Thermo-hydro-mechanical microscopic changes in shales further influence the macroscopic behavior and reliability of the host rock for deep geologic disposal. Such consequences are observed through long term creep experiments which that suggest that the primary failure mechanism of shale changes from pressure solution processes to micro-rupture processes as stresses increase (Geng et al. 2016, Zhang 2018).

It is important to also mention the role of water content on the observed behavior of shale. Stiffness, dilatancy, and ultimate compressive strength are observed to decrease significantly with increasing water content (Blümling et al. 2007, Zhang 2018). As the water content in shale increases, swelling causes the distance between clay particles increases resulting in decreased frictional resistance. Lu et al. (2017) observed that the water weakening affect is heavily influenced

by clay content and temperature in saturated rocks by performing compressive tests on mudstone and sandstone. At elevated temperatures, the water content in the mudstone was shown to increase significantly resulting in a diminished compressive strength due to the water weakening effect while sandstone was shown to have a reduction in water content as temperatures increased resulting in an increase in compressive strength. This suggests that the mechanical strength of shale is highly coupled with the clay content as well as water content.

Despite various research efforts, the THM characteristics of shale due to time-dependent microstructural changes are still poorly understood, especially at large time scales. For these reasons, it is important to further study how thermomechanical processes affect the microstructure and the macroscopic properties of shale. The experimental results should then be used to calibrate existing numerical models to simulate shale systems over long time periods.

2.2 Mock HE

The primary objective when developing HE material is to balance the optimization of explosive performance and minimize susceptibility to various forms of insults that could result in damage or ignition (Herman et al. 2021). The properties of HE materials are heavily dependent on the microstructure characteristics such as binder properties and crystal quality and size distribution. In addition, recycling HE materials due to high manufacturing costs has been shown to significantly affect the thermo-mechanical properties and performance of the HE (Peterson and Idar 2005). Experiments necessary for the characterization of virgin and recycled HE are expensive; therefore, HE is often replaced by “mock” materials that are dependent on many of the same factors as the HE materials. With the application of high-pressure thermal triaxial testing, the thermo-mechanical properties of mock HEs can be provided for the computational models attempting to simulate the behavior of such material.

The triaxial testing used to investigate the behavior of shale can also be utilized for the testing of mock HE material. Ideally, the mock HE matches the thermomechanical response (i.e. density, stress-strain curvature, and temperature dependency) of the real HE. Yeager et al. (2020) performed uniaxial compression on Mock 900-21 and Mock Idox at various temperatures. The results are shown in Figure 2.3 and were compared to identical tests performed on actual high explosive material (PBX 9501). These materials are relatively soft but exhibit the tendency to be stiffer and stronger at lower temperatures.

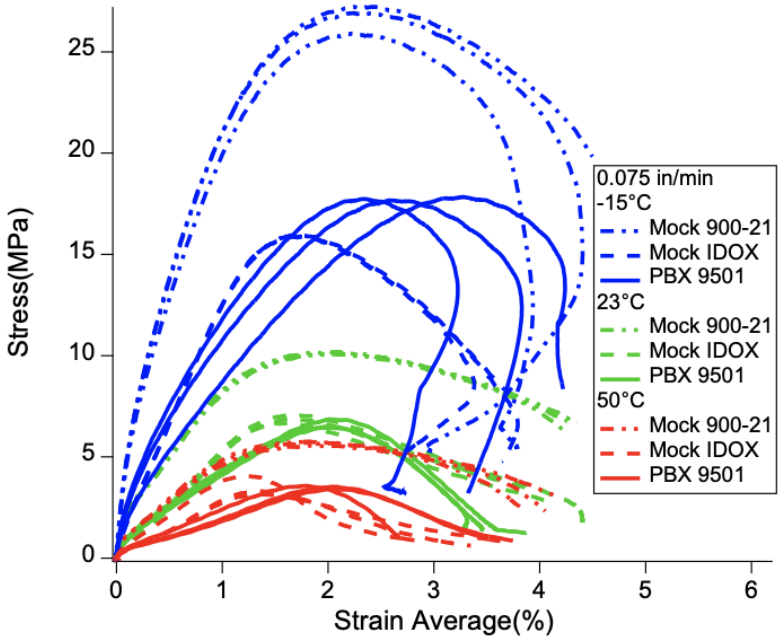

Figure 2.3: Stress-strain data for uniaxial compression test performed at different temperatures (image from Yeager (2020))

While these tests demonstrate the macroscopic behavior of these materials under uniaxial loading conditions, there remains a lack of data on how confining pressures may affect these results. Confining pressure effects can alter the response of the material when subjected to various loading paths observed at different temperatures. These effects are therefore relevant for understanding the complete thermo-mechanical behavior of the material.

It is understood that the thermomechanical behavior of high explosives is dependent on whether the samples are virgin or recycled. Recycled lots are typically produced due to the expensive nature of the explosive components, such as TATB crystals, used for plastically bonded explosive (PBX) production. Peterson and Idar (2005) suggested that differences in the failure mode and temperature variations are linked to the differences in the microstructure between the virgin and recycled lots. They observed that the TATB crystal were smaller and more homogenously distributed in sampled pressed using recycled lots compared to the samples produced with the virgin lots. These differences are observed in Figure 2.4.

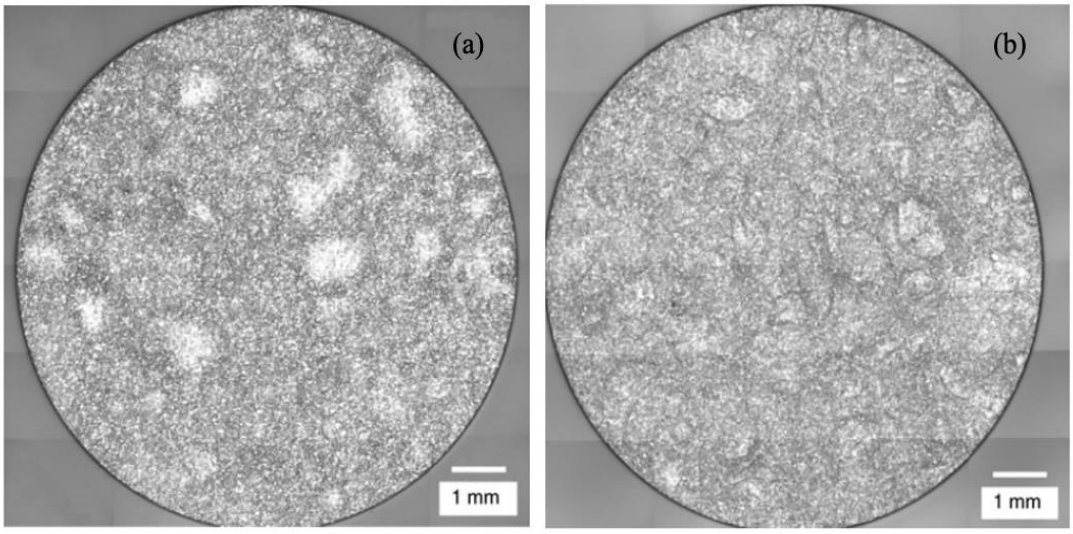

Figure 2.4: Polarized light microscopy images for (a) virgin PBX 9502 lots (b) recycled PBX 9502 lots (images from Peterson et al. (2005))

To match these differences, it's important to select mock and recycled mock materials that exhibit the same trends as the real PBX material. Particle size selection and processing temperature during the manufacturing of the mock samples are shown to significantly influence the materials strength and stress-strain behavior (Herman et al. 2021). Additionally, recycling these samples will alter the particle size and an appropriate recycled mock to be representative of the recycled PBX. High pressure thermal triaxial testing on the virgin and recycled mock HE will provide more insight on

how closely the mocks exhibit the trends observed in the real HE material and aid in the development of engineering models.

CHAPTER 3: EQUIPMENT COMPONENTS AND DEBUGGING

3.1 Basic Components

The MTS 815 triaxial machine at the University of Colorado Boulder integrates several main components and systems to conduct high-pressure and high-temperature triaxial tests on high-strength materials. These components include a load frame and chamber, a confining fluid filtration system, hydraulic fluid system, a servo-controller rack, heating elements, and a computer. The machine has the capability of performing tests up to confining pressures of 140 MPa and temperatures up to 120°C.

The frame is fed by high-pressure hydraulic fluid to raise and lower the chamber and move the frame to apply axial loads on specimens. The confining fluid filtration system allows confining fluid to be supplied to the device. If the fluid becomes contaminated with sediments, the operator can use the system to run the fluid through a filter until the fluid becomes clear. The fluid system is controlled by valves on a rack located adjacent to the load frame. The system consists of a pump, a manual valve to divert fluid to the chamber or to the filter, a filter, an alarm system if the filter element becomes clogged, and a fluid holding tank. Access to the hydraulic pumping system and actuators is also located on this panel. The system consists of three different types of piston actuators: (1) load actuator, (2) confining pressure actuator, and (3) pore pressure actuator. At the time testing was performed using this machine, leakage was observed from the pore pressure actuator and it was therefore sealed off from the rest of the system. A schematic of the filtration and hydraulic fluid system is shown in Figure 3.1. The orange line located at valve 3 transports confining fluid to and from the chamber. The orange lines at valve 5 and valve 6 transports pore fluid to and from the top and bottom of the specimen. The blue lines filter the fluid. The operational procedure for using this system will be discussed in Chapter 4.

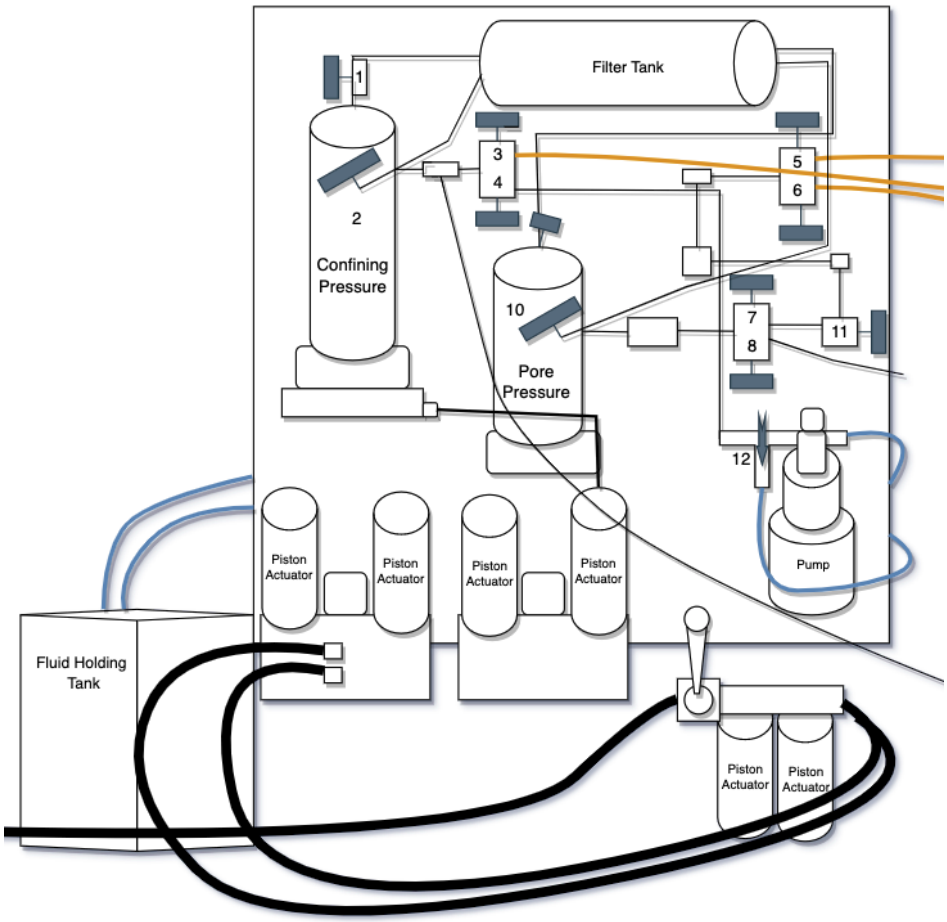

Figure 3.1: Fluid filtration and hydraulic pumping system

The servo-controller rack allows for the manual control of the frame position, confining pressure, pore fluid pressure, and temperature. The manual operation of these elements is typically used during the setup process when initial loading and temperature conditions are applied. Each control type is given an individual panel with a viewing window to read the voltage values obtained from sensors in the testing frame. When using the manual mode, the center knob can be switched to "SETPOINT" to view the target voltage. When the knob is pointed towards "FEEDBACK", the viewing window displays the current voltage value reported by the sensors. Coarse and fine adjustment knobs allow for the user to reach and fine tune the desired voltage numbers during the setup process. Each panel also consists of a small knob allowing for operators to change the control mode for each control type. The frame actuator can be controlled by frame displacement (using an

LVDT located under the testing frame) or by load control which uses a load cell located inside the test chamber. Both the confining pressure intensifier and pore pressure intensifier can be controlled by volume control or pressure control. There is a third control mode labeled “other” for each intensifier, allowing for additional control modes to be added in the future. A schematic of the servo controller is shown in Figure 3.2.

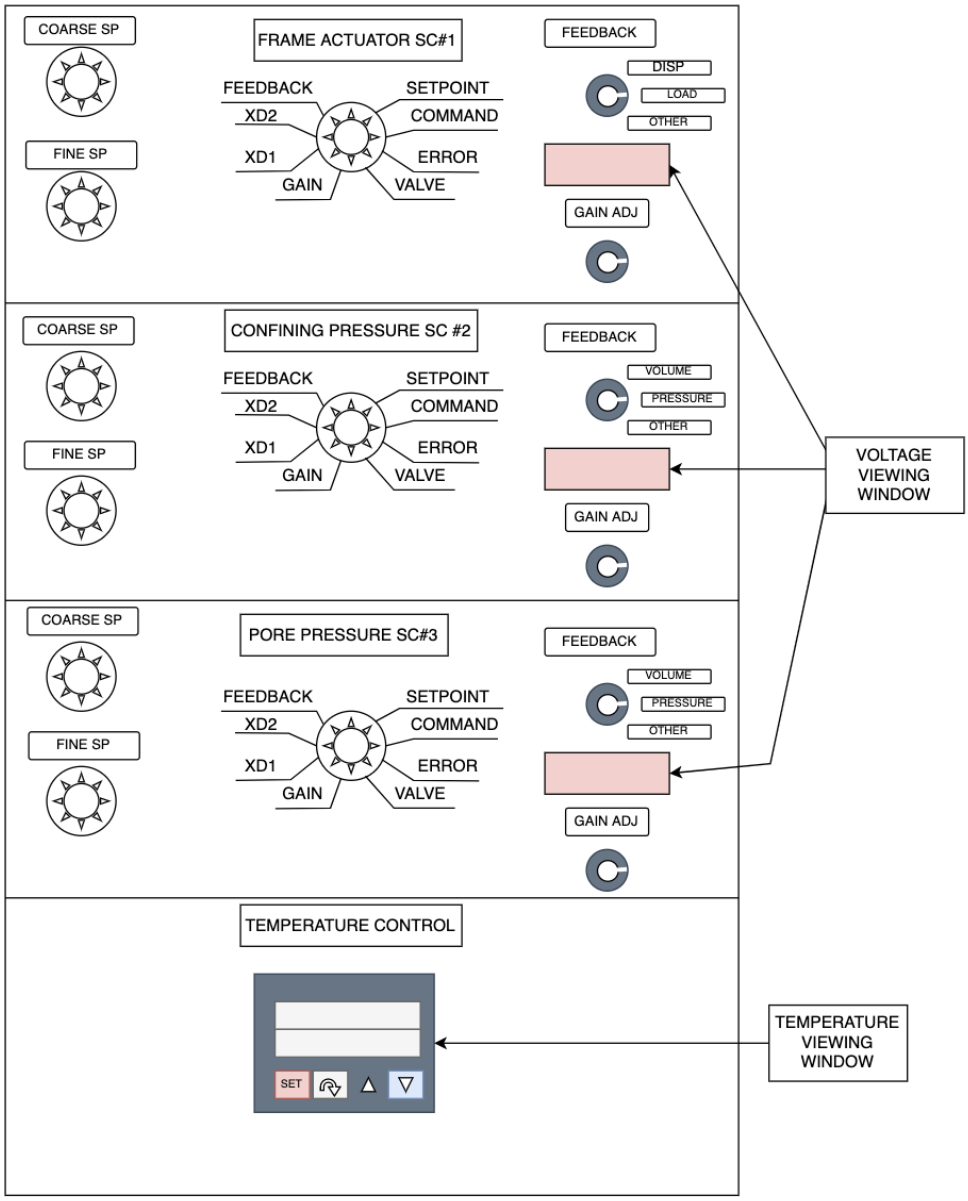

Figure 3.2: Servo-controller rack for manual operations

There were several drawbacks to using this servo-controller system. The setup did not allow for the change between force control and displacement control during pre-loading or testing without bringing the voltage value back to zero and consequently unloading the sample completely. Experimental set up with the manual knobs can also be confusing and can easily result in sample damage prior to testing. A new system is under development that does not include such manual components. The new system will allow for setup and testing to be solely conducted through a LabVIEW user interface on the computer.

LabVIEW is the primary software used to design and run tests. The user interface is divided into several main tabs. The data acquisition tab allows for real time visualization of senor readings. The Build Profile tab is used to design the confining pressure, pore pressure, and load or displacement over time when building tests. The Test Execution tab allows for real time plotting of desired values such as stress vs strain data. The proposed updated interface includes an additional set up window for user input of exact initial condition values which will relay information to the servo-controller and be implemented by the intensifiers.

Several key components located inside the chamber are required to collect sample data and perform tests. The load cell is primarily used for the collection of the axial load data. Two sensors are mount on the sample, one is an axial extensometer which measures axial deformations and another one is a circumferential extensometer that measures changes in sample circumference. Along the base of the chamber exists several other connections including a heating element power connection, thermocouple connections, and connections for the load cell and strain sensors. Figure 3.3 demonstrates a simple setup of the components located inside the chamber.

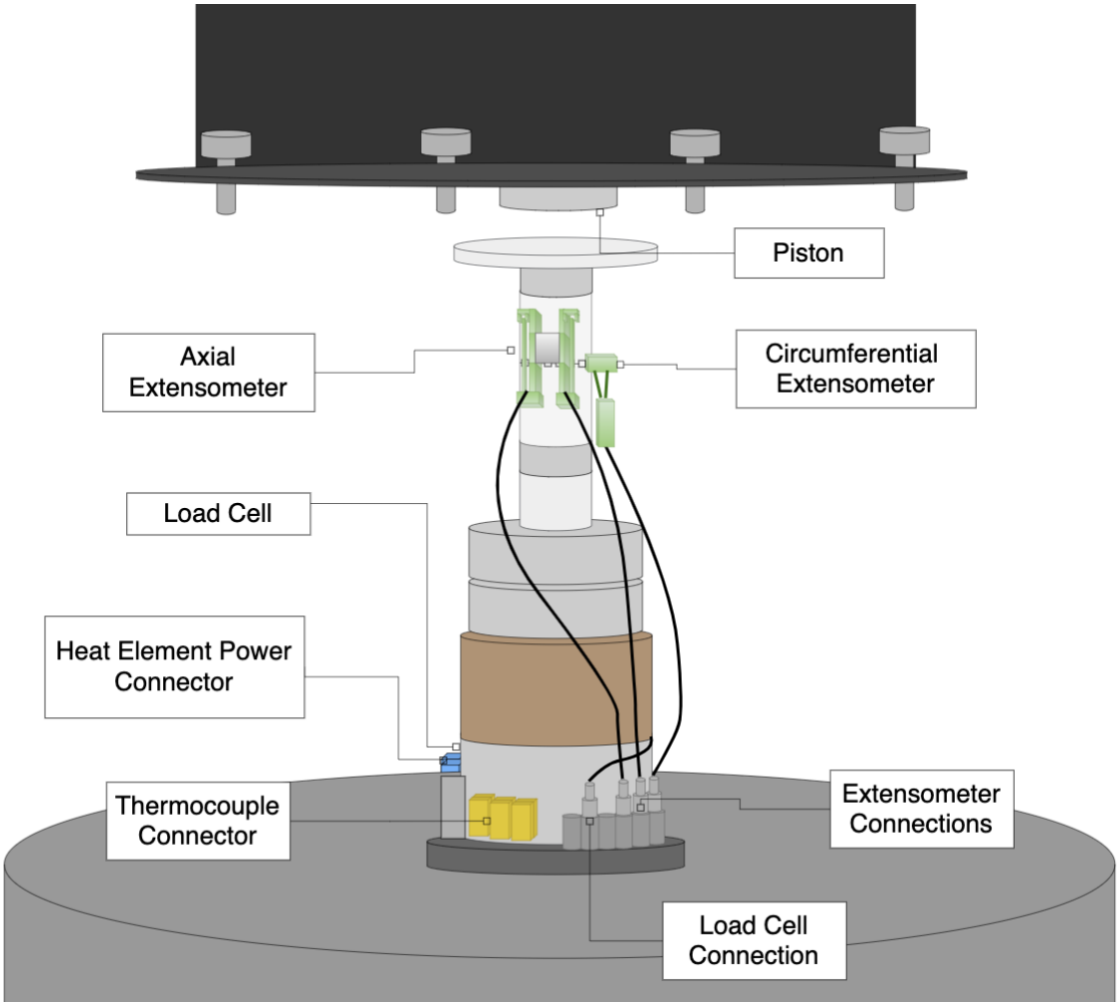

Figure 3.3: Triaxial testing equipment located inside chamber

3.2 Debugging: Load Cell and Confining Pressure Effects

The CUBoulder high pressure triaxial device was completely reequipped with new electronics, fluid, and hydraulics systems, making it necessary to perform preliminary tests and complete debugging. Such tests were performed on dummy Mancos Shale specimens. The first issue observed was the shifting of load cell readings when confining pressures were applied. A test design was constructed to automate confining pressure changes while holding either the load or frame displacement constant. The confining pressure for both tests was first increased to 5 MPa and then decrease the confining pressure back to 0 MPa. Under force-controlled condition, the test

program was designed to maintain the initial axial preload as the confining pressure changed. It was observed that during these tests the test frame moved upward as the confining pressure increased and moved downward as the confining pressure decreased. Displacement-controlled tests were then performed and designed to maintain 0 mm of displacement as the confining pressure was applied. As the confining pressure increased, the load cell reading slowly decreased and then maintained a constant load around 0 MPa before it increased again as the confining pressure decreased. When the load approached zero and remained constant, it was determined that the top of the sample had lost contact with the upper loading platen.

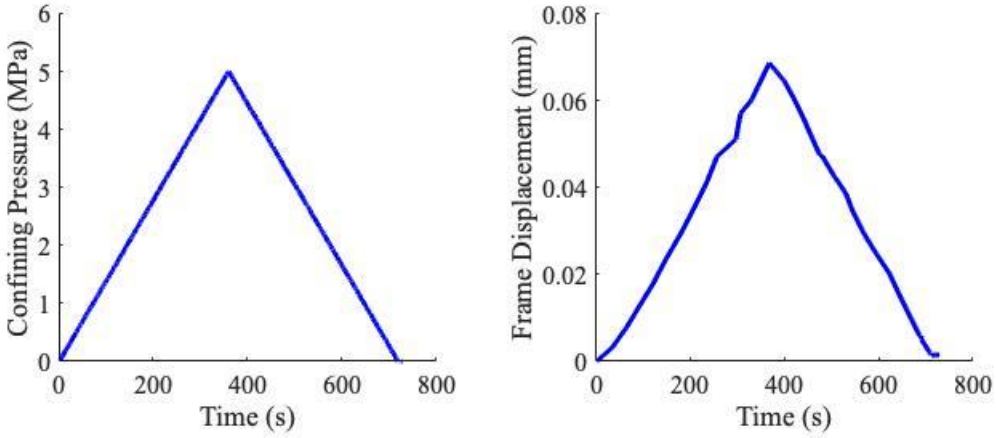

Figure 3.4:Frame displacement response to pressure change under force-controlled conditions

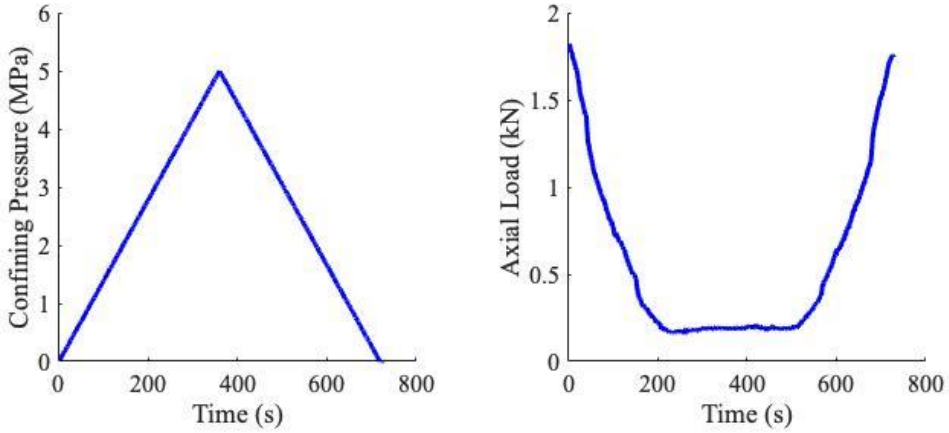

Figure 3.5: Axial load response to confining pressure change under displacement-controlled conditions

To confirm that the load cell alone was not influenced by the increase in confining pressure, an additional displacement-controlled test was conducted without a specimen, such that only confining fluid was present within the chamber. The confining pressure was increased to 45 MPa while the load cell readings were monitored. The results are show minimal changes in axial load with dramatic changes in confining pressure (Figure 3.6).

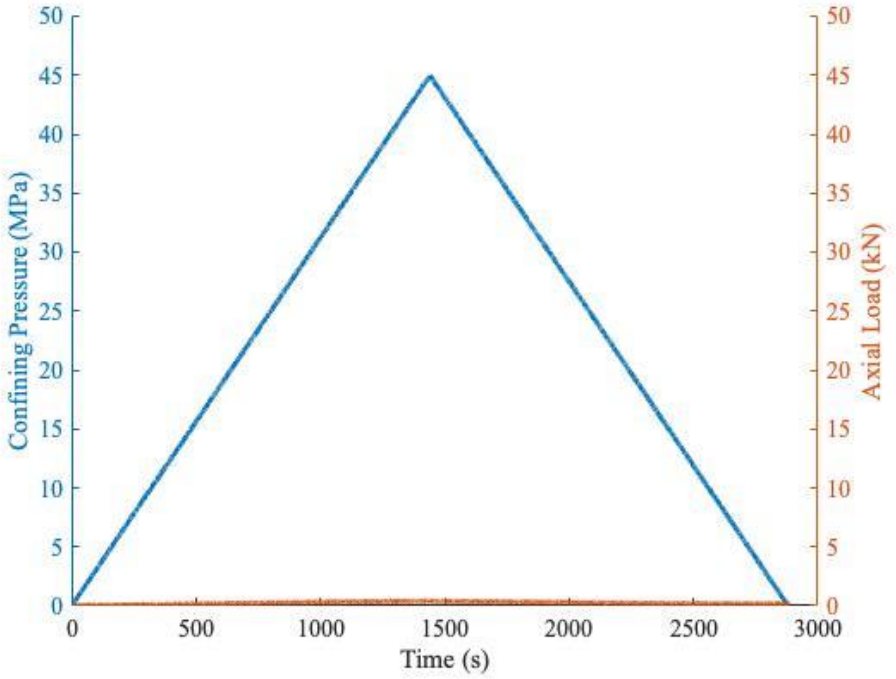

Figure 3.6: Axial load readings during confining pressure change without sample

We found it intriguing that the confining pressure and axial load cell readings are independent when there is no specimen, but they become highly coupled when a sample is loaded. We therefore hypothesized that this effect is due to confining fluid getting in the gap between the loading platen and sample. The presence of the fluid within the gaps results in the confining pressure sharing some of the axial load imposed on the sample. A schematic of this hypothesis is depicted below in Figure 3.7.

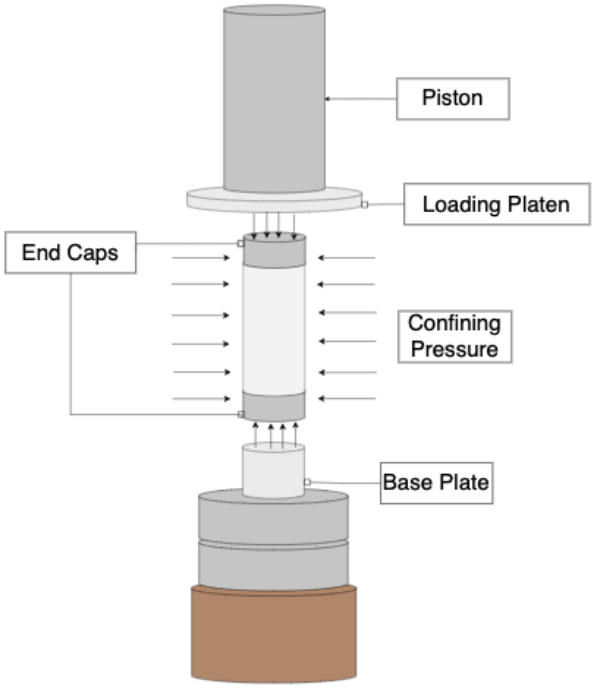

Figure 3.7: Schematic of confining fluid compressing specimen

When the confining pressure was applied, the specimen experienced isotropic compression. During the displacement-controlled tests the sample was axially compressed due to the increase in confining pressure which resulted in a decrease in load cell reading until contact with the load piston and top platen is lost. During the force-controlled test, the machine attempted to compensate for this decrease in force by increasing the frame position as observed in Figure 3.4. Based on these results, the true axial stress should be calculated using Equation 3.1, which is used for all the data processing in this thesis.

$$\sigma_a = \sigma_p + \sigma_c \qquad (3.1)$$

Here, σ_a is the actual axial stress experienced by the specimen, $\sigma_p$is the axial stress provided by the piston, and σ_c is the confining pressure. This equation assumes that a thin layer of fluid completely separates the end cap and platens.

It must be emphasized that the coupling between the confining pressure and axial load cell reading is not well understood. A more systematic investigation on this issue should be carried out in the future on other dummy samples such as aluminum, which do not experience deformations under isotropic loading conditions. For the experimental procedure presented in this thesis, the confining pressure will be applied manually with the data acquisition open such that the load is observable, and the desired axial preload is maintained.

3.3 Force-Controlled Tests Versus Displacement-Controlled Tests

It was initially speculated that displacement control would result in a bigger data scatter since this control mode relies on signals from the native LVDT in the axial actuator located outside of the testing chamber which is quite aged. Conversely, the load cell is newly installed and located inside the chamber right beneath the sample, which can give a better signal for the axial force servocontrol. However, it is soon realized that load- or stress-controlled test have several disadvantages when performing quasi-static compression tests. For instance, under force-controlled tests, strain softening curves were impossible to obtain because the machine directly follows the instruction of the program to continue increasing the force at a predetermined rate. When the specimen fails and is unable to withstand additional load, the frame continues to move upward trying to obtain a larger force and the rate at which the frame moves upward increases. This leads to an appearance of a plateau in the stress-strain curve while, when in fact, the material may be experiencing strain softening.

Several force-controlled tests were performed on Mancos Shale specimens and compared to results obtained from strain-controlled tests conducted on similar shale samples by Masri et al. (2014). The results from our tests appeared to show a ductile behavior without any strain softening (Figure 3.8) while Masri et al. (2014) observed a strain softening after the peak. This led to the conclusion

that the force-controlled test results were not representative of the post-peak material behavior. Furthermore, the failed specimens from our tests completely crumbled, and post-test visual inspection of cracks and planes of weakness was impossible.

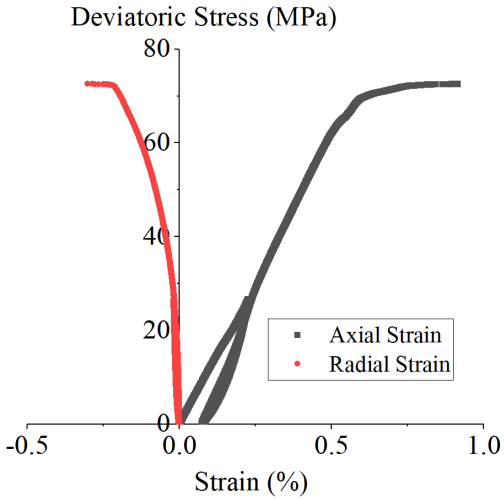

Figure 3.8: Force-controlled test performed at a confining pressure of 5 MPa on vertically bedded sample

Displacement-controlled tests were then conducted on the shale specimens. It was found that the LVDT performed better than expected and the full strain softening response of the specimens were able to be captured (Figure 3.9). The resolution of the LVDT reading may be insufficient at very small stress levels, an effect that should be considered when the axial load is below 10 kN.

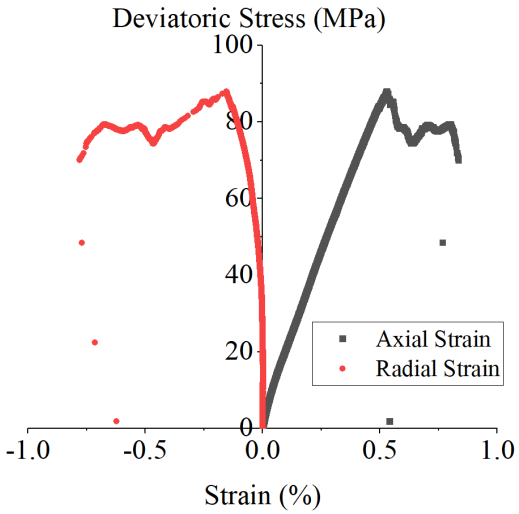

Figure 3.9: Displacement controlled test performed at a confining pressure of 5MPa on vertically bedded sample

Ultimately, both testing procedures have their own benefits. The displacement-controlled tests are best suited for tests where specimens are quasi-statically loaded to past peak till complete failure. On the other hand, force-controlled testing is necessary when studying long-term creep behaviors of the material where a constant load is required. Since the load cell has excellent resolution, it is expected that these tests will produce reliable results.

3.4 High Temperature Tests

The final challenge to overcome, was heating the thermal confining fluid inside the chamber to conduct high-temperature tests. When placing the heating element in the chamber, there were many wires that were difficult to keep out of the way when lowering the chamber. As a result, one of the wires was crushed during one of the trial tests, causing the heating element to short circuit and damage several other elements within the machine. A surge protector has since been installed externally to the chamber to prevent a similar issue from occurring in the future. The heating element was also replaced with a new element consisting of a hollow metal cylinder, heating fabric, and power connection. The same connection as the old element is used and a Teflon sheet is placed inside the element to prevent other wires from contacting the heating element and melting. The cylindrical shape also allows the heating element to surround all the wires and essentially protect the internal wires from crushing when the chamber is lowered, as shown in Figure 3.9b. Finally, the thermal fluid can be heated significantly faster with the new element. It now takes only one hour to heat the chamber to 50 °C when previously this heating process needed to be completed overnight. Above 50 °C the heating process does still need to be done overnight and an insulating box should be placed around the machine. With overnight testing, the setup is monitored by a camera that can be remotely accessed. The Team Viewer software is used to access the computer remotely if issues are detected during overnight testing.

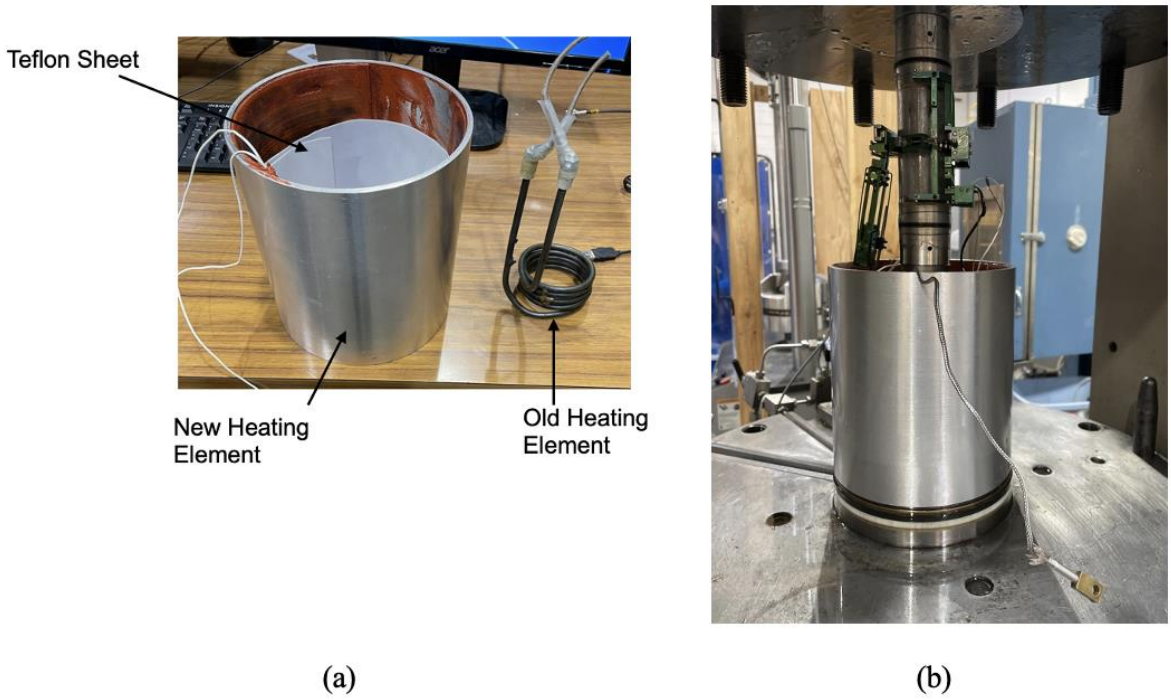

Figure 3.10: Images of (a) new heating element compared to old element and (b) installation of new heating element

Once the new heating element was successfully calibrated and installed, it was found that as the temperature of the thermal fluid increased, the axial stress on the specimen also increased due to the expansion of the sample and other metal components within the machine. Upon further testing, it was found that the axial stress increased by about 1 MPa for every 2°C increase in temperature. To avoid this issue, the sample was raised to a height with significant room between the sample and loading platen such that any thermal expansion would not lead to a vertical stress increase on the sample. The axial preload was then applied when the target temperature was arrived.

A new method is also needed when heating the fluid such that the thermal liquid could expand without affecting the confining pressure. Due to plastic tubing at the top of the triaxial machine with a maximum temperature limit of 60°C, the upper valves of the chamber could not be left open to simply release excess pressure due to fluid expansion. Therefore, the only way around is to let

the servo-controller for the confining pressure intensifier to adjust the confining pressure in the machine as the confining fluid is heated up. The chamber is first filled with thermal fluid, and before closing all valves to apply confining pressure to the specimen, the confining pressure intensifier is turned on. Using volume control, the piston is moved to about a third of the maximum height to give the actuator to have enough range of motion in both directions to adjust the confining pressure based on fluid expansion (or fluid contraction when the heating element is turned off). The top valves are then closed, and the desired amount of confining pressure is applied to the specimen using the servo controller. The desired temperature of the chamber is then set, and heating begins. Once the desired temperature is reached, the frame is raised to bring the sample in contact with the top platen and the preload is given. The preparation stage is now complete, and the official testing program is ready to begin.

CHAPTER 4: OPERATIONAL PROCEDURES

4.1 Experimental Setup

The following sections outline the procedures taken to set up high-pressure thermal triaxial experiments. Specific discussions are also made on some changes implemented when performing high temperature tests. The purpose of this section is to outline the steps that should be taken by anyone who plans to work with the CUBoulder MTS 815 Triaxial Device.

4.1.1 Sample Preparation

In early trial tests, a significant amount of oil contamination was observed on each of the samples tested. It was observed that oil contamination was significantly worse for specimens exposed to higher levels of confining pressure for longer durations. From these initial tests, it was clear that the heat shrink membrane alone used for testing was not sufficient to keep the sample sealed. Oil contamination, especially if oil were to soak into the sample, could lead to test results that do not reflect the true behavior of the material under investigation. The oil could also cause some materials to dissolve, which was especially an issue for the Mancos Shale samples.

To further improve the contamination, O-rings are placed on the metal caps and after each test the O-rings are replaced to ensure a proper seal between the heat shrink membrane and end caps. The sharp edges of the metal where the O-rings are placed can result in the tearing of the membrane, so a generous amount of vacuum grease is applied around the O-rings to lubricate and further seal the crevasses where the O-ring sits. After the heat shrink membrane is applied, metal wire is tightened around either side of the O-rings carefully to ensure additional sealing.

Another adjustment is made by closing pore pressure fluid holes at the top and bottom end caps that are positioned on either end of the specimen during loading. The current testing set up and

machine does not use pore pressure, and not plugging the cap holes allows for oil to pass through the caps and contaminates the specimen. After the membrane is positioned and heated, two screws are used to plug the pore pressure holes in the specimen caps. This new sample preparation is shown in Figure 4.1.

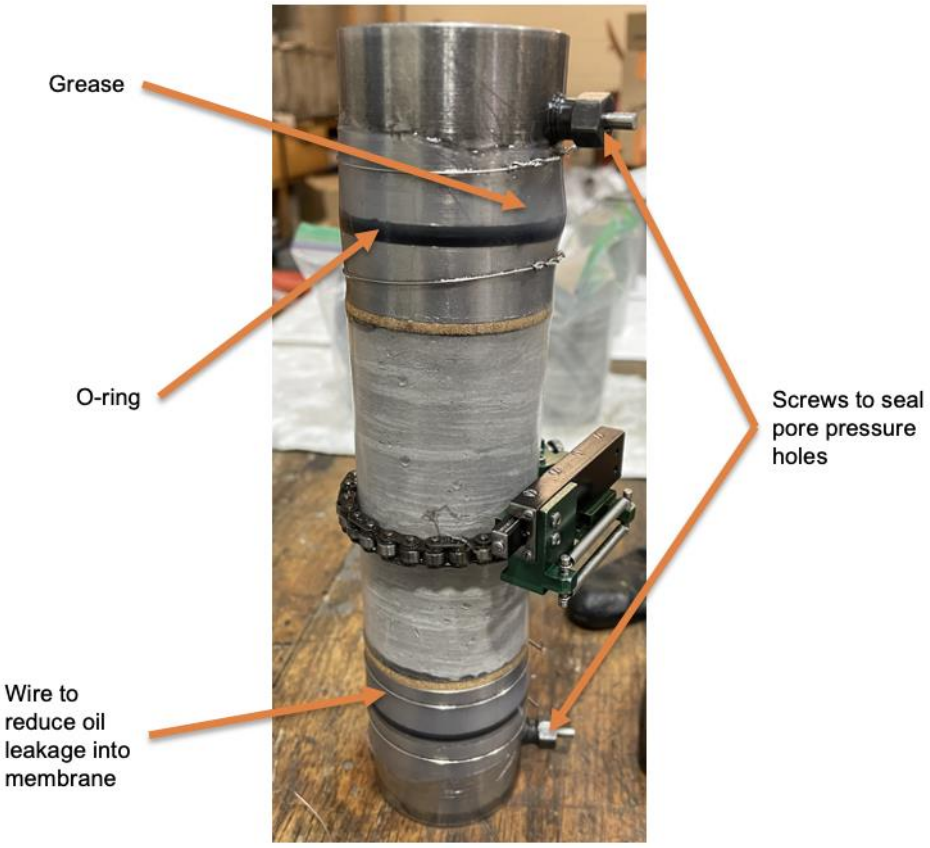

Figure 4.1: Sample preparation techniques

Since the implementation of this sample preparation procedure, the oil contamination has been minimized and oil is no longer observed on the surface of the specimen after testing, even at high confining pressures. Figure 4.2 shows the improvement made with this procedure, with the first image showing the sample heavily contaminated due to poor sealing technique and the second showing a properly prepared sample without any oil contamination after testing.

(a) (b)

Figure 4.2: (a) Specimen contaminated with oil (b) clean specimen after testing with improved preparation method

After the appropriate measures are taken to reduce sample contamination, the specimen is instrumented with displacement sensors. The testing setup uses two different displacement sensors. A custom roller chain is installed around the center of the specimen and adjusted by two small screws to ensure a secure fit. An extensometer is then inserted below the spring mechanism attached to the chain to monitor circumference changes. This extensometer connects to a port within the testing chamber which sends information to the computer regarding these changes. The second gauge straddles the chain wrapped around the specimen's diameter and measures axial deformations. Two sets of pins secure the sensor to the sample. The arms of the extensometer are aligned before testing to a zero position. When the sample is loaded, the arms are allowed to rotate, and the gauge measures the amount of axial displacement of the sample through the arm. The gauge connects to two ports within the confining chamber to relay strain information to the computer.

The sample, top and bottom end caps, and sensors are all placed inside the chamber. A loading platen is placed on top of the top end cap to properly distribute the load from the piston to the sample without damaging the top cap or piston due to differing sizes. If high temperature testing is desired, a heating element, thermocouples, and a Teflon sheet is also placed inside the chamber before inserting the sample. Before applying any loads to the sample or lowering the test frame chamber, all senor wires are examined to ensure they are out of the way of the chamber and will not be damaged or crushed.

4.1.2 Applying Preload to Specimen

It is often desirable to apply some amount of preload to the specimen to secure the sample's position and initial state. The preload is applied manually using the servo-controller system either before or after lowering the chamber. First it is ensured that the "SET POINT" voltage reading displayed on the servo-controller viewing window was below 0 V. Next, the knob above the viewing window is switched to the desired control type. Once selected, the load actuator is turned on from the computer by selecting the "Hyd Low Actuator" then "Hyd High Actuator" buttons located at the bottom of the LabVIEW window. The voltage is then adjusted on the serv-controller to the value desired.

4.1.3 Applying Confining Pressure

When elevated temperatures or confining pressure is required for testing, the chamber is closed and filled with confining fluid. It is of critical importance that no air remains in the chamber and that the chamber is completely sealed before applying any type of confining pressure. Improper usage could lead to large leaks or explosion.

The chamber is controlled by two knobs to the right-hand side of the load frame. Opening one knob allowed for the frame to be raised while the other allowed for the frame to be lowered. It is important to ensure that both knobs are closed once the desired chamber position was reached. Only one knob is opened at a time, and the amount that the nob is rotated affects the rate at which the chamber raised or lowered. When closing the chamber, the speed of the chamber is reduced as it approaches the bottom of the sample to ensure that none of the internal wires from the machine are in the way of the chamber. Once lowered, the bolts secure the chamber to the bottom of the frame.

Next, the chamber is filled with liquid. Before entering the chamber, a small pump that circulates the liquid is turned on to eliminate any air bubbles that may exist within the tube connections. Once there are no more bubbles seen in the clear storage tank that, the top valve of the chamber is opened, and the small lever located at the top of the chamber is pointed to towards the plastic tube that leaves the chamber. This is where the fluid exits the chamber and allows for air to be pushed out as the chamber fills. The valves on the panel next to the machine are then opened to allow the fluid to flow into the chamber. If everything is working properly, bubbles can be observed exiting the clear plastic tube leaving the top of the chamber.

The fluid flows through the system until no more bubbles are visible in clear plastic tube. Sometimes the fluid will stop flowing when the pump pushing the fluid into the machine stalls or additional fluid is needed for the system to continue pumping fluid to the tank. To restart the pump, the pump is turned off then turned back on. When necessary, fluid can be added to the system by pouring fluid into the storage chamber. Once the chamber is filled, the valve at the top of the chamber is slowly closed while examining the plastic tubing exiting the camber to observe if any remaining air bubbles leave the chamber. If air bubbles are present, fluid should continue to run

through the system before closing the valves. If no bubbles are observed, the valve is fully closed, and the fluid pump is shut off.

The confining pressure is then applied to the chamber using pressure control. Similar to the frame actuator, the confining pressure actuator is turned on through LabView from “Low” to “High”. With the data acquisition monitor open, the confining pressure is applied manually using the nobs on the servo-controller in the confining pressure panel. Once set to the desired confining pressure, the servo controller automates adjustments to location of the piston within the confining pressure intensifier to maintain the desired pressure. After running any test, the voltage value is reduced to 0 on the servo-controller to remove all confining pressure within the system.

4.2 Design and Run Test

LabView is used to generate csv files that are used to define and run all MTS 815 triaxial experiments. To design each test, the control mode (displacement or force) must first be defined by adjusting the voltage conversion values and units in the system configuration window shown in Figure 4.3. The values displayed in this window are based on the calibrations performed on all sensors and the load cell. Since the displacement LVDT and load cell require different voltage conversions for their respective values, the units, slope, and y-intercept next to “Channel 0” under “Other AO Scaling” must be changed whenever switching between displacement-control and force-control tests.

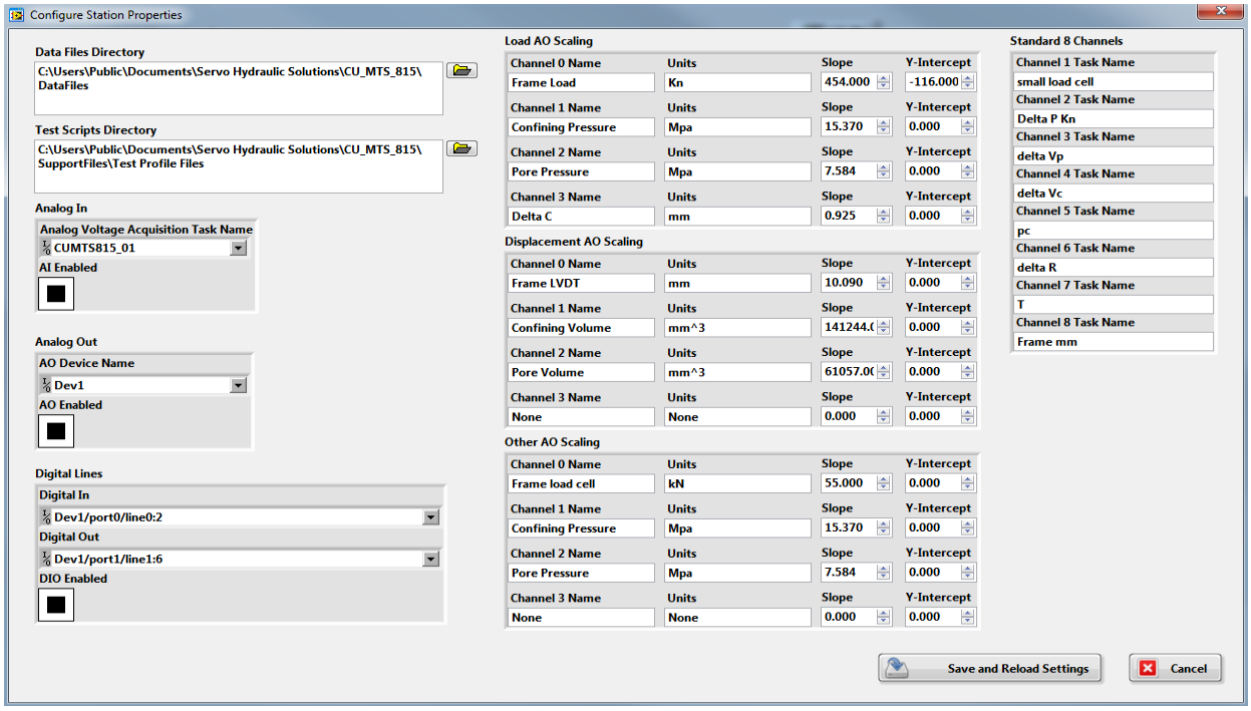

Figure 4.3: System configuration window

Once these test configuration values and units are defined, the Build Profile tab (Figure 4.4) is used to design each test. This tab allows for profiles to be loaded or created. The saved profiles are read by the computer and relayed to the servo-controller when testing begins.

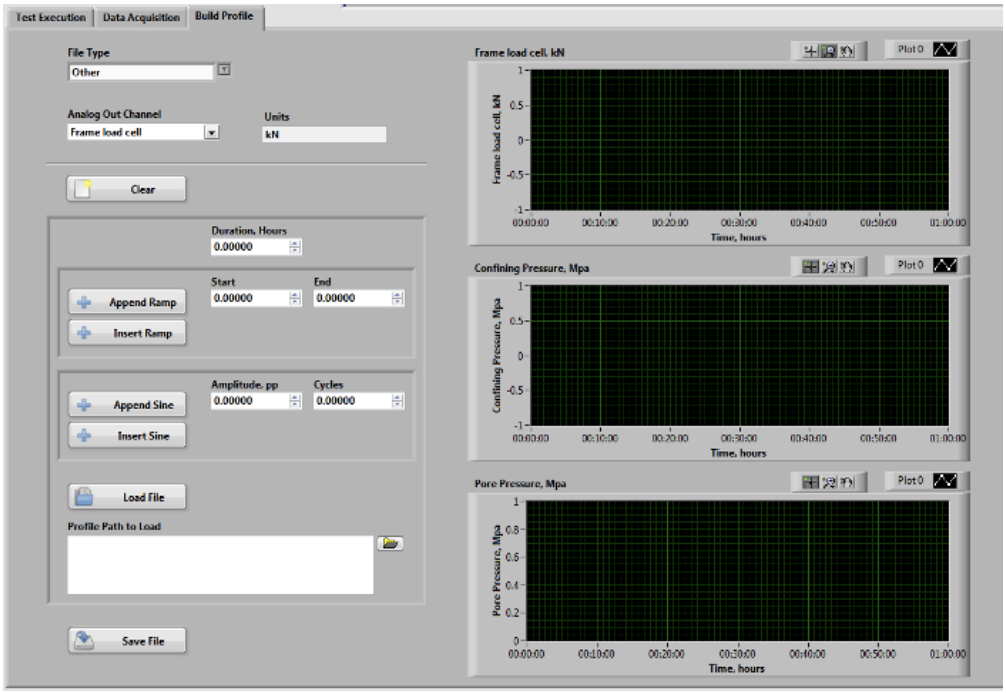

Figure 4.4: Build Profile tab for test design

The units next to each channel plot will change based on what was defined in the system configurations window. Since the values are associated with “Other AO Scaling”, the “Other” file type is selected for all tests regardless of the control mode. The frame displacement or force, confining pressure, and pore pressure make up the three channels that define the testing profile. A channel is first selected in the “Analog Out Channel” dropdown menu. Segments are then added to each channel in the profile by appending ramps and adding start and end values over a given duration in hours. All test channel profiles designs have initial values of 0. The program uses the values assigned during the manual setup process as this initial zeroed value. It is important that all channels are given values over the same total interval, or the profile will not save. Due to leakage issues, pore pressure was not applied to the sample, but the pore pressure channel profile was still assigned values of 0 over the entire testing duration.

> ***Example:*** An operator applies a 2 kN preload and a confining pressure of 20 MPa to a test specimen prior to running a test. The operator wants to increase the load from 2 kN to 10 kN over 6 minutes then decrease the load back to 2 kN over an additional 6 minutes while maintaining the 20 MPa confining pressure. The operator builds this profile by selecting “Other” as the file type then selecting “Frame load cell” in the analog output channel drop down. The operator then types 0.1 into the duration (which is equivalent to 6 minutes), then types 0 for the start point and 8 for the end points and clicks “Append Ramp”. Using the same duration, the operator then types 8 for the start point and 0 for end and clicks “Append Ramp”. The frame load cell design window should now show the design ramping from 0 kN to 8 kN and back down to 0 kN over a total time of 0.2 hours. When running the test, the initial value of the ramp will start from the initial preload applied and the actual load will peak at 10 kN. Following a similar procedure, the confining pressure channel will be

designed to remain at 0 MPa for the entire 12-minute (0.2 hour) duration which will result int the confining pressure maintaining 20 MPa for the entire test. The pore pressure should also be designed to maintain 0 MPa for the entire duration.

Once designed, the test profiles are given a file name and saved. The profile is then loaded on the left-hand side of the user interface and a name for the output file is assigned under "Test Data File Name". The "Sample Inputs" button is selected to input the initial sample dimensions. In special cases, specific channels are selected to stop the test if a given value is exceeded. For instance, if it is desired to stop the test immediately if the sample experienced a vertical displacement of 1 mm, a channel can be toggled to "On" and the Delta L channel measuring the axial displacement, the comparison "Greater Than", the engineering value of 1mm, and the action of "Stop" are selected from the appropriate drop-down menus located next to the channel. This window is shown in Figure 4.5.

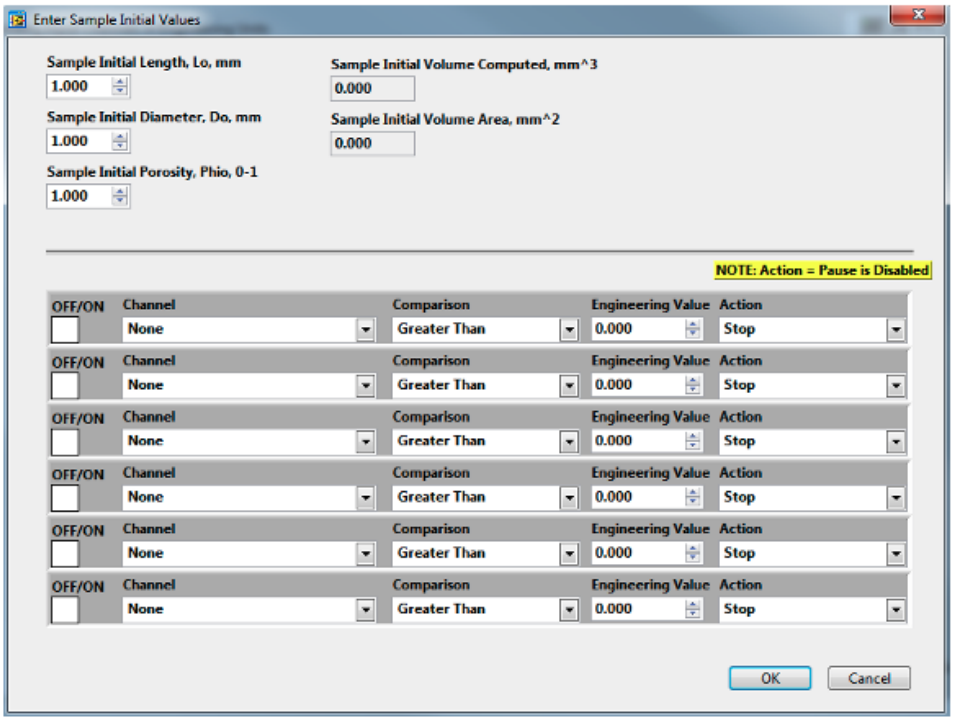

Figure 4.5: Initial sample values window

Once the test profile is loaded and all sample inputs are provided to the program, the operator can run the test. The Data Acquisition tab allows for the visualization of different measurements during testing. Different visualizations are toggled on and off by selecting different sensor selections located on the right-hand side of the viewing window. In the case that something goes wrong during a test, there are several measures to stop the testing. In cases where the threat of personal danger or damage is low, the "STOP TEST" button should be selected, and the system will slowly return to the initial load conditions set before running the test. When person safety or machine damage is of major concern, there is a physical emergency stop button located next to the machine that manually forces the machine to reduce all pressures. There is also an E-Stop button on the LabVIEW user interface that can be selected if the mechanical button does not work. As a last measure, the hydraulic pressure valves located at the back of the machine can be closed to prevent the frame from continuing to move upward. A screenshot of the data acquisition tab is shown in Figure 4.6 below.

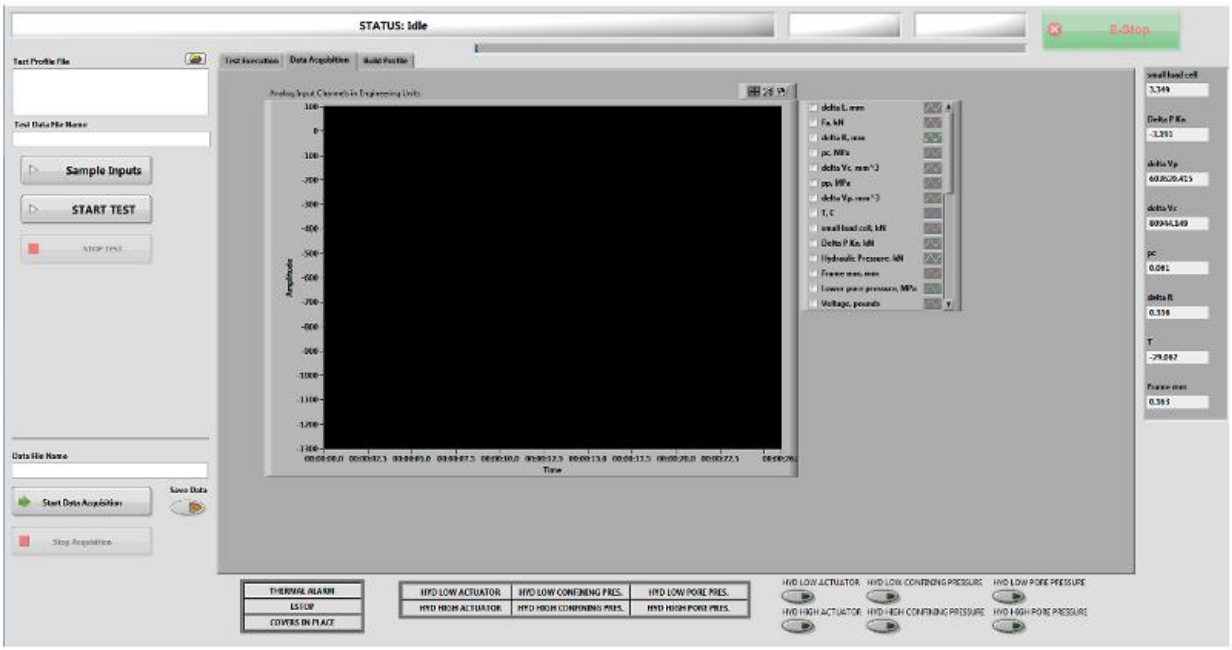

Figure 4.6: Data Acquisition tab

4.3 Removal of Liquid and Sample

After any test where confining pressure or elevated temperature is applied to the sample, the confining fluid within the chamber must be removed. First, the system is manually relieved of all confining pressure and the actuator is shut off from the LabView interface. Next the valves that allow the fluid to run from beneath the tank back to the holding tank are opened. An air hose is then connected to the top valve on the chamber and the valve is opened allowing air from the hose to push the fluid out of the chamber. Once the fluid in the holding tank begins to bubble indicating all fluid has been removed, the hose is detached, and all excess air is allowed to escape the chamber to depressurize any remaining air pressure. All screws at the bottom of the frame are loosened and the knobs to the left of the machine are used to raise the chamber. The knobs are completely tightened once the chamber is fully raised. Finally, the specimen is removed, and all gages are disconnected and stored.

4.4 High Temperature Tests

As previously discussed, it was observed that the confining pressure and axial load increased if the fluid filtration valves are closed when heating the elements within the chamber for high temperature tests. Furthermore, it was required that the filtration valves were closed to ensure that air bubble did not enter or melt the plastic tubing leaving the chamber as fluid expanded due to the temperature increase. These additional requirements for the adjusted procedure are discussed below.

After the sample was installed in the machine with the heating element surrounding it, a thermocouple is attached to the top of the specimen to monitor the temperature within the chamber. This thermocouple relays temperature information to the servo-controller which adjusts the power

supplied to the heating element. Because of limited space within the chamber, none of thermocouple attachments are used to relay temperature information to the computer for recording; this was however not a concern since the temperature was constant during testing. After the sensors are installed, the test frame is raised such that the sample rests several millimeters below the loading piston. This allows for the elements beneath the piston to expand without exerting additional stress on the specimen. The chamber is then lowered and the procedure to fill the chamber with liquid is followed. The valves on the filtration rack behind the machine are closed while the top valve on the chamber is left open. Leaving this valve open allows for the piston within the confining pressure intensifier to adjust without increasing the confining pressure.

To adjust the piston position, the confining pressure control mode is switched to volume control. The confining pressure actuator is turned on and the voltage is increased manually to about 3V which moves the intensifier piston about 1/3 of the way up from the bottom position. At this point there is no confining pressure within the chamber. The valve above the chamber is then closed such that the confining pressure can be set for the test. After closing the top valve, the confining pressure control mode is switched to “pressure” without turning off the actuator, and the voltage was quickly lowered manually to obtain the desired pressure. The piston now has full range of motion to move and maintain the desired confining pressure during heating.

The desired temperature is next set using the temperature control at the bottom of the servo-controller. The sample is left overnight to reach the desired temperatures above 50 °C. Once the temperature is met, the preload can be applied manually and the procedures to run the test were performed. After testing, the system is allowed several hours to cool down before removing the liquid and sample from the chamber.

CHAPTER 5: MANCOS SHALE EXPERIMENTAL RESULTS

5.1 Introduction

This chapter reports the results of a series of thermal-triaxial tests on Mancos Shale samples with axial load perpendicular to the plane of lamination. The tests were performed at elevated temperatures between room temperature and 80 °C and confining pressures ranging from 5 MPa to 20 MPa.

5.2 Sample Material

Mancos Shale samples from the San Juan Basin located in southern Colorado and northwestern New Mexico were studied for this study. The samples used for mechanical testing in this report were 2 in in diameter by 4 in in height and cored perpendicular to the plane of lamination and provided by the Kocurek Industries INC. XDR analysis indicated that the sample minerology was composed of roughly 57% silicates, 18% carbonates, 24% clay minerals, and trace amounts of Pyrite by mass (Wang et al. 2021).

Prior to testing, samples were stored at room temperature in plastic wrap to preserve the natural water content of the Mancos Shale. During sample preparation, the shale specimens were placed between two metal end caps. Due to groves present on both of the end caps, sintered porous metal discs were placed between the end caps and shale to evenly disperse the load over the specimen. A heat shrink wrap was secured over the sample, porous metal discs, and end caps to prevent thermal fluid from entering the shale material. Metal wire, O-rings, and grease were used to further ensure a tight seal to prevent oil intrusion.

5.3 Mechanical Testing Procedure

For high temperature test, a heating element collar was installed around the sample and a thermocouple was tightened to the top end cap to monitor and automate temperature adjustments. After installing the sample within the chamber, the chamber was filled with thermal fluid and the desired confining pressure was manually applied. The desired temperature was then increased with the sample free of any load. After the temperature to equilibrated, a preload of about 1 kN was applied to the specimen manually.

The unloading/reloading behavior of the shale was studied by loading each sample to approximately 50% of the peak deviatoric stress, then unloading the sample completely before reloading the sample to failure. Table 5.1 summarizes the frame displacement values and deviatoric stress at which each sample was unloaded.

Table 5.1: Frame displacements and deviatoric stress at beginning of unloading phase

Confining Pressure (MPa)	Temperature (°C)	Frame Displacement at Unloading (mm)	Deviatoric Stress at Unloading (MPa)
5	20	0.9	45.3
	50	0.65	27.2
	80	0.8	39.3
10	20	1.0	54.6
	50	0.9	36.0
	80	1.0	58.2
20	20	1.1	61.9
	50	1.2	77.1
	80	1.2	70.1

Initial monotonic tests were performed on samples confining pressure of 5 MPa, 10 MPa, and 20 MPa, allowing for an approximation of the axial displacement required for the sample to reach 50% peak stress for unloading. The full unloading/reloading tests were performed at confining pressures of 5 MPa, 10 MPa, and 20 MPa for each temperature 20 °C, 50 °C, and 80 °C, for a total of 9 tests. A strain rate of 10^{-6} /s was used for all triaxial compression tests and data was collected at 1 second intervals.

5.4 Results and Discussion

The results show a clear dependence on confining pressure as expected. When comparing the results of all nine tests, it is observed that the measurements taken at 50 °C are not very reliable. This was likely due to the axial extensometer becoming loose dur to the expansion of the metal tension spring when the temperature was increased. The extensometer was adjusted to have a better fit on the sample for tests conducted at 80°C. Due to the limitation in the number of horizontally bedded samples, additional testing at 50 °C was unable to be reperformed. Analysis and discussion will primarily focus on the observed changes between temperatures of 20°C and 80°C. Further testing at 50°C will provide more insight on how the gradual change in temperature influences the mechanical behavior of Mancos Shale. The stress-strain results for each temperature at the three confining pressures are plotted in Figure 5.1. These plots indicate that the 20° C and 80° C test allow for a better interpretation of the thermo-mechanical trends exhibited by the material.

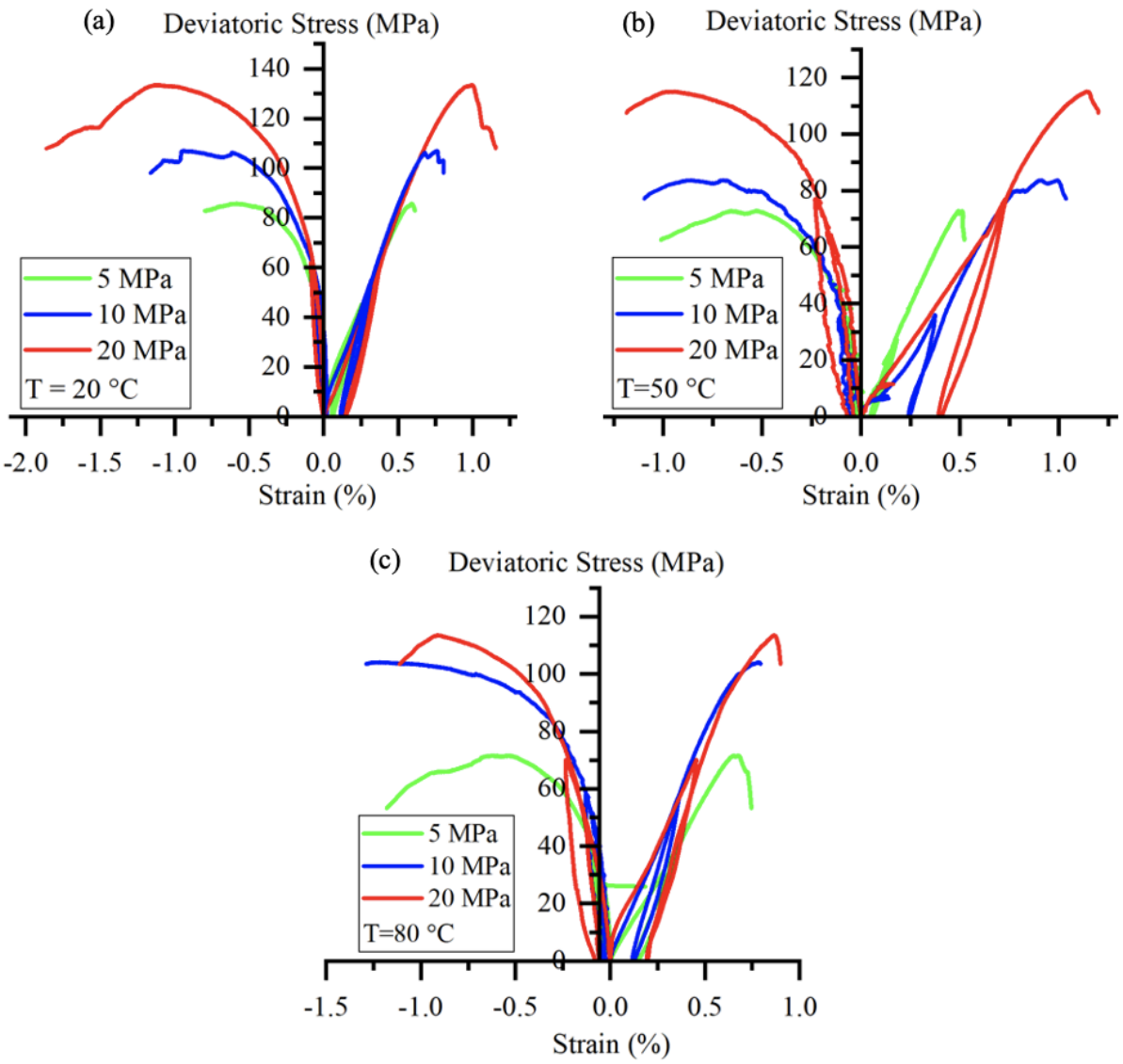

Figure 5.1: Stress strain curves at temperatures of (a) 20°C (b) 50°C and (c) 80°C

Figure 5.2 plots the results due to the variation in temperature presented at each confining pressure. The figure also plots the same results with the 50 °C test results removed. The results show a clear dependence of the shale's mechanical behavior on temperature. The Young's modulus was observed to decrease slightly with increasing temperature while compressive strengths of the shale specimens were observed to decrease with increasing temperature.

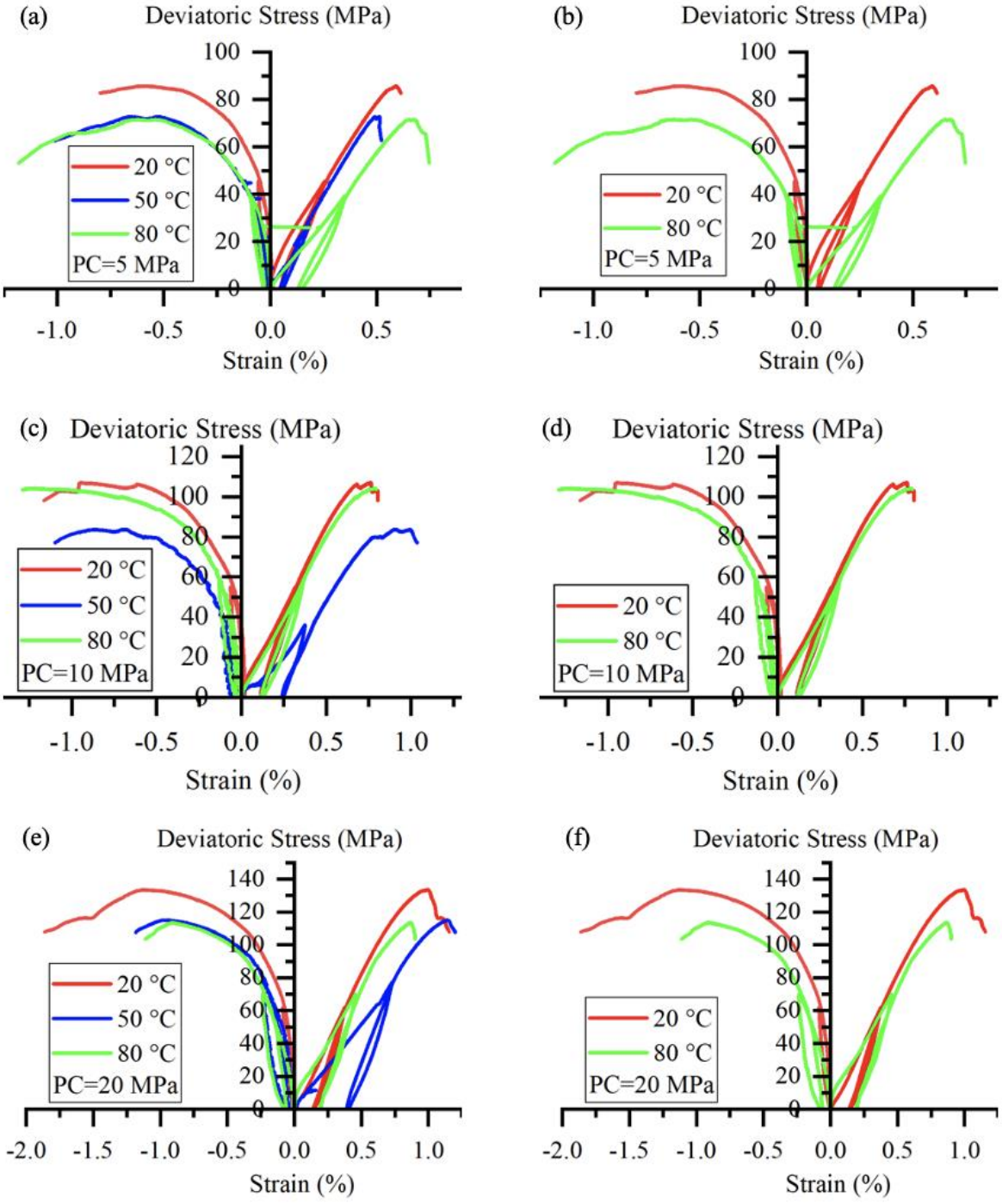

Figure 5.2: Stress Strain curves exposed to different temperatures for confining pressures of (a, b) 5 MPa (c, d) 10MPa and (e, f) 20MPa

The results show a clear dependence of the shale's mechanical behavior on temperature. The Young's modulus was observed to decrease slightly with increasing temperature while compressive strengths of the shale specimens were observed to decrease with increasing temperature. These values are summarized in Table 5.2.

Table 5.2: Peak deviatoric stress and Young's Modulus for all tested specimens

Confining Pressure (MPa)	Temperature (°C)	Peak Deviatoric Stress (MPa)	Young's Modulus (MPa)
5	20	85.1	16641
	50	72.3	15573
	80	71.6	11480
10	20	106.1	17082
	50	83.0	11108
	80	104.1	16159
20	20	132.4	16368
	50	114.2	10321
	80	113.6	14998

The change in Young's Modulus at elevated temperatures reflects a softened elastic response of the shale samples. At lower temperatures, the shale experienced a stiffer response. Masri et al (2014) observed similar results for Tournemire Shale and determined that there is a strong dependency of anisotropy on the Young's Modulus.

The temperature dependency of peak stress is also believed to be dependent on both the water content and clay content. For saturated specimens, the water content increases for higher clay content rocks at elevated temperatures and decreases for low clay content rocks (Lu et al. 2017).

The peak stresses observed by Lu et al. (2017) are influenced the saturated water content due to the water weakening effect, with decreases in peak stress observed at elevated temperatures for high clay content saturated rocks and increases in peak stress is observed at elevated temperatures for low clay content saturated rocks. Samples prepared for this study were tested at the natural saturation state which could potentially affect the mechanical behavior of the shale specimens at elevated temperatures (Blümling et al. 2007, Zhang 2018).

The novelty of this study comes from the examination of the unloading/reloading response from the specimens to observe the changes in the hysteresis due to temperature. The unloading elastic modulus, E_U, and the reloading modulus, E_R, are shown in Table 5.3 for temperatures of 20°C and 80°C. It was observed that there is a slight decrease in both moduli at elevated temperatures.

Table 5.3: Unloading and reloading moduli at temperatures of 20°C and 80°C

Confining Pressure (MPa)	Temperature (°C)	E_U (MPa)	E_R (MPa)
5	20	27.4	18.2
	80	24.0	16.3
10	20	33.5	23.1
	80	33.4	21.9
20	20	35.1	24.6
	80	25.5	21.4

Figure 5.3 presents the volumetric strain versus axial strain data. The total volumetric strain for each sample studied experiences an initial contractive response followed by a dilative response, which is typical for rocks and over-consolidated clays. The initial contractive phase results from the elastic compression of the sample causing microcracks generation and damage growth within

the sample. The followed dilation response can be understood by the "sawtooth" model as the microcracks are sheared and coalesced. During unloading, the sample relaxes but some permanent strain remains, resulting in permanent volumetric strain. Upon reloading, and exceeding the unloading strain value, the microcracks continue to grow until the mode of damage changes over to dilatancy. The microcracks grow and propagate at an accelerating rate until the sample fails. The results at all temperatures show that larger confining pressures produce greater compressive volumetric strains followed by lower dilative phases as axial strain is increased.

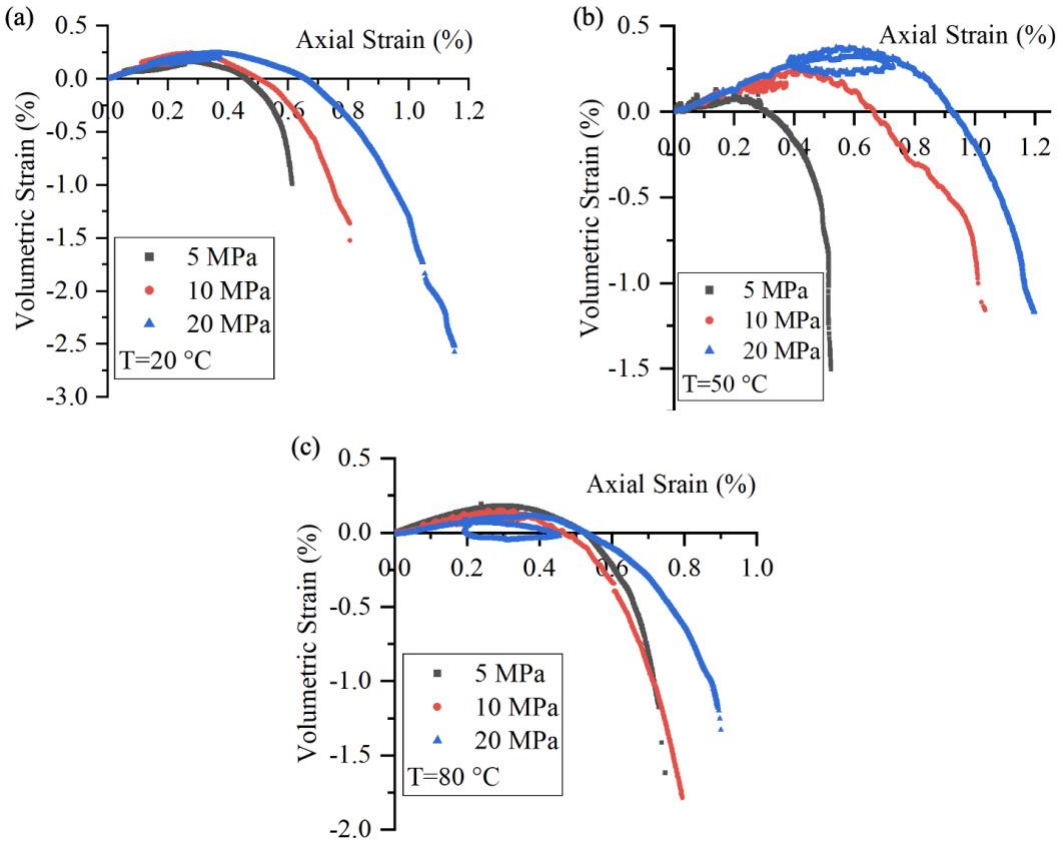

Figure 5.3: Volumetric strain at temperatures of (a) 20 °C, (b) 50 °C, and (c) 80 °C

Figure 5.4 displays the axial strain versus volumetric strain observed at different temperatures under the same confining pressures. Due to the unreliable axial strain measurements of the 50 °C tests, the adjacent plots display results only for tests performed at 20 °C and 80 °C. The effect of temperature on the volumetric behavior of shale is very minor. It seems that at low-confining-

pressure levels, higher temperature postpones the dilation phase, while at high-pressure levels the trend is reversed. The physical and micromechanical reasons behind this trend needs to be further investigated.

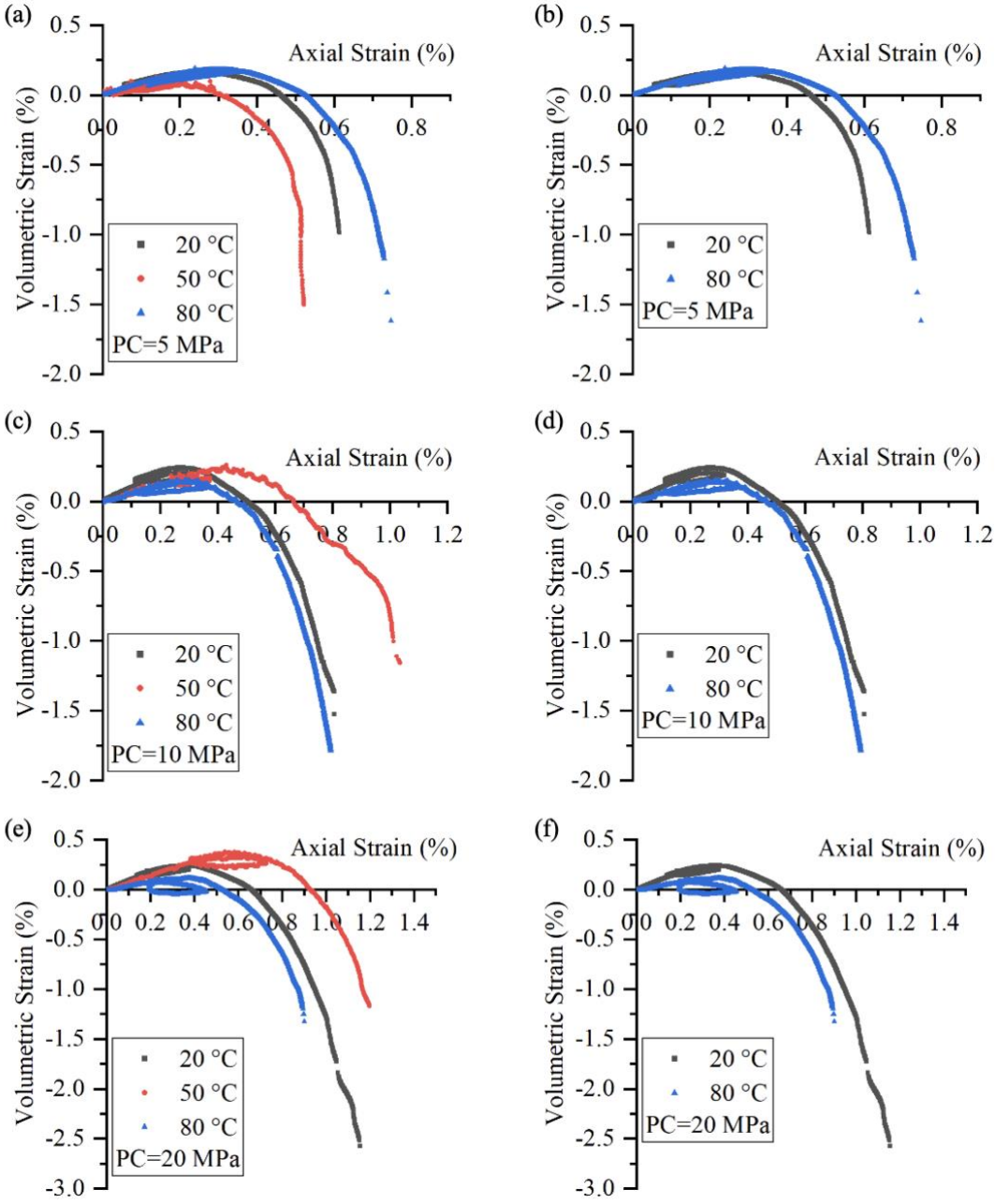

Figure 5.4: Volumetric curves at different temperatures for confining pressures of (a, b) 5 MPa, (c, d) 10 MPa, and (e, f) 20 MPa

CHAPTER 6: PERMEABILITY TESTS

6.1 Permeability of Shale

The permeability of rocks is typically determined by permeating fluids such as inert gas or water through the sample to provide information about the rock's transport properties (Paterson and Wong 2005). These properties are dependent on both the pore volume and connectivity of the porous space and are significantly dependent on the mean effective pressure it is subject to. Samples exposed to high pore pressures or low confining pressure result in larger permeabilities (Brace et al. 1968). Additionally, with an increase in deviatoric stress, the permeability of shale samples should also increase (Wang and Zhang 2021) due to the formation of microcracks and level of damage in the specimen. The permeability of shale is also highly anisotropic due to its anisotropic microstructures which defines preferential flow of fluid through pore spaces and generated cracks (Kwon et al. 2004).

Properly containing the HWL within deep geologic structures is heavily influenced by the transport properties of the host rock. It is therefore important to understand the evolution of permeability in shale rock under changing stress conditions. The focus of this chapter is to explore how the permeability of shale specimens is affected by different levels of damage created by loading to different levels of deviatoric stress.

6.2 Sample Preparation

Permeability tests were performed on four vertically bedded Mancos Shale samples. Three of these samples were loaded to either 30%, 60%, or 90% of the peak deviatoric stress and then unloaded. All three samples were loaded at room temperature with a confining pressure of 5 MPa. A fourth sample remained unloaded as a reference sample for the permeability tests. Figure 6.1 shows the

initial failure test which was used to calculate the displacement at which each sample should be unloaded.

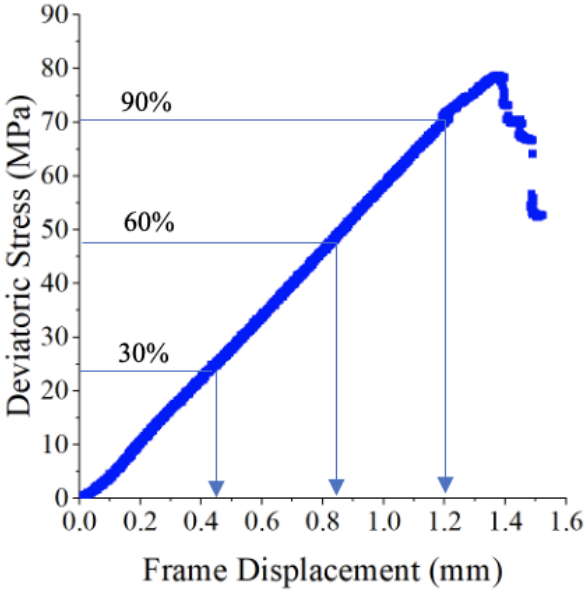

Figure 6.1: Frame displacement determination for unloading samples

The unloaded test results for each sample are shown in Figure 6.2, and Table 6.1 summarizes the targeted unloading stress and the actual unloading deviatoric stress for each sample.

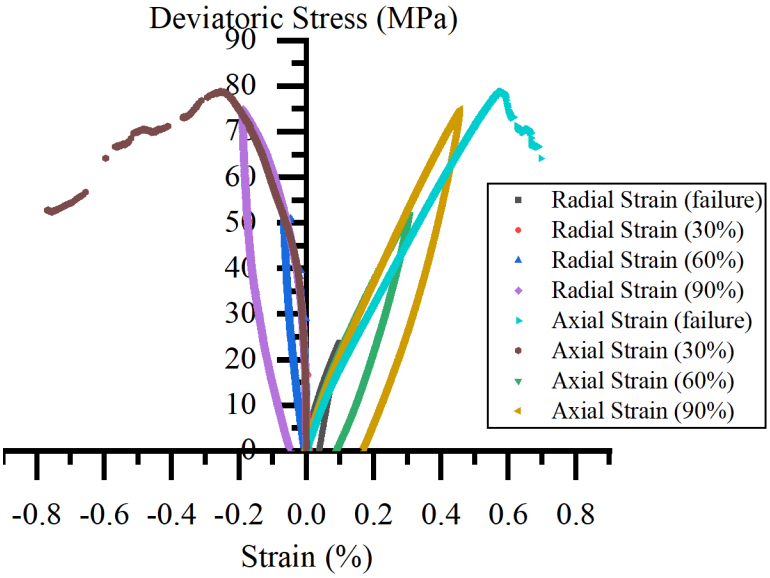

Figure 6.2: Stress strain curves for unloaded samples

Table 6.1: Deviatoric stresses at beginning of unloading phase for strain-controlled tests

Unloading %	Design Maximum Displacement (mm)	Target Deviatoric Unloading Stress (MPa)	Actual Deviatoric Unloading Stress (MPa)
30	0.47	23.6	23.7
60	0.85	47.2	51.7
90	1.2	70.8	74.8

Permeability tests were performed using the CMS-300 permeameter at the Colorado School of Mines. The test allowed for the calculation of pore volume, porosity, and permeability for each sample. The CMS-3000 requires the samples to be between 0.75 inches to 3.5 inches in length and 1.45 inches to 1.55 inches in diameter; therefore, after the initial 2-inch by 4-inch samples were prepared at different loading conditions, they were cut to achieve this size requirement.

Typically, with larger initial block samples, coring devices are used to obtain smaller samples. However, due to the brittle behavior of shale and the small amount of material that needed to be removed from each sample, other methods of cutting were utilized to reduce the sample sizes. A lathe at the Colorado School of Mines was used to slowly remove material from each sample to reduce the diameters. Each sample was secured between two metal ends of a lathe that rotated the sample about its axial axis. The device was secured to an end grinder using a strong magnet preventing the device from moving during cutting. Figure 6.3 shows the lathe and end grinder that was used to cut the samples and its basic components.

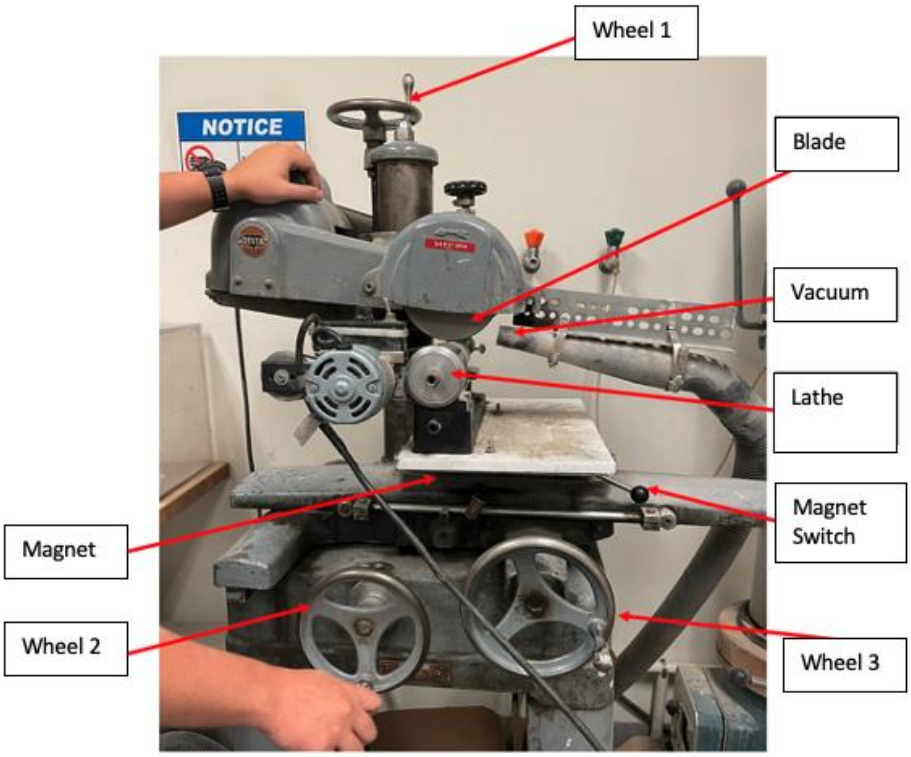

Figure 6.3: Image of end grinder and lathe components used for reducing sample diameters

The end grinder consists of three main wheels. The top wheel (Wheel 1) adjusts the height of the blade that will cut the spinning sample. The wheel was turned about $1/5^{th}$ of a revolution to remove about 0.04 inches off the diameter per pass. The left wheel (Wheel 2) moves the lathe holding the sample perpendicular to the blade, allowing material to be removed along the length of the sample. The bottom right most wheel (Wheel 3) allowed the lathe holding the sample to be moved parallel to the pin direction of the blade. This allowed the sample to be centered with the blade before cutting began. A vacuum to the left of the blade was used to collect airborne dust generated by the cutting processes.

During initial cutting, some wobble was observed as the sample rotated. This wobble was slowly removed as cutting continued. If too much material is removed at once or the sample is pushed too quickly along the blade, the sample could be moved off its initial axis and wobble would be

observed again. This should be avoided to avoid cutting too much material off the specimen or throwing the specimen off the device.

When cutting the sample that was unloaded at 60% the peak deviatoric stress, it was observed that one of the bearings on the lathe had failed and was not rotating the specimen properly, which caused the sample to get sudden wobble during cutting. Figure 6.4 shows the location of the bearing failure. Due to this failure, too much material was removed from the specimen and one of the ends of the specimen fractured when removing it from the device. The final diameter of this sample was 1.4465 inches which was 0.0035 inches short of the range that could be used for the permeability test. However, because this error was so small, the sample was still successfully tested.

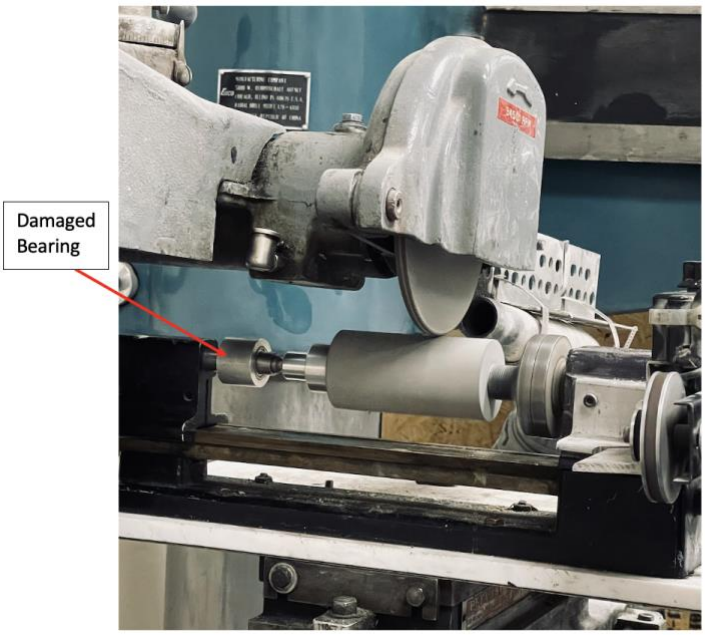

Figure 6.4: Location of damaged bearing from side view

After each sample was cut to a diameter in the proper range for the permeability test, each sample was the cut to reduce the specimen length. A low-speed diamond saw was used to slowly cut the sample. The sample was lowered on to the saw and pressed against the blade with its own self-

weight. When the blade was almost fully through the sample slight upward pressure by hand was provided to obtain a smooth finish and avoid bending the blade. Figure 6.5 shows an image of the diamond saw used to cut the sample.

Figure 6.5: Image of saw used to reduce length of vertically bedded specimens for permeability testing

Figure 6.6 displays the final cutting results for each loading case. The sample on the far left shows the initial sample size for reference. For each loading case the sample with the smoothest cutting result was used for the permeability test. The samples used are on the left side for each loading condition. As shown above, the 60% loaded case has a much longer sample length due to the fracture created during the diameter reduction process. Only a small amount of the 60% loaded case was cut to avoid the risk of ruining the entire sample if the crack continued to propagate.

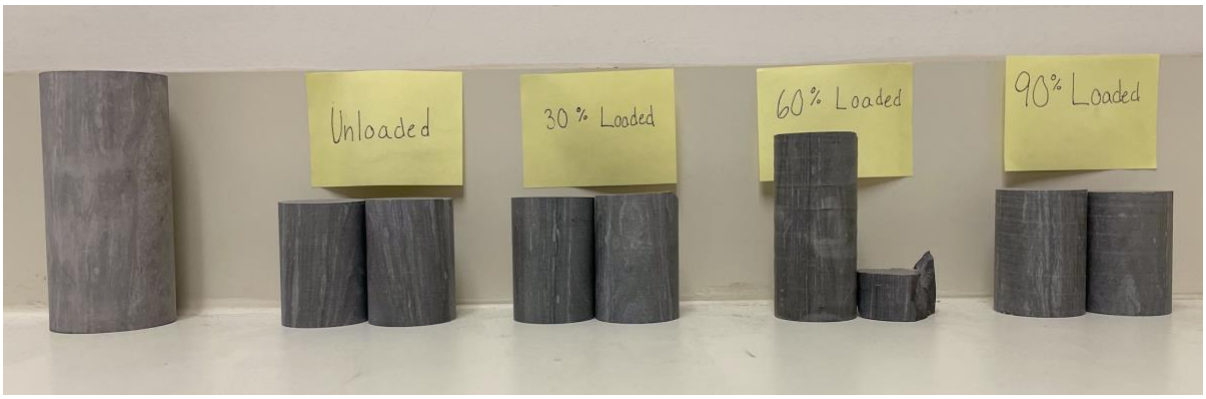

Figure 6.6: Image of cut samples and initial uncut sample size

6.3 Permeability Testing and Results

The samples were tested in the CMS-300 permeameter one at a time. For each test nitrogen was used to predict the permeability and porosity. The device performs a quick test to estimate the permeability before running the official test. If the check determines the permeability is greater than 0.05 md, then the device switches from using nitrogen to using helium gas for permeability testing. Figure 6.7 shows an image of the permeameter used to obtain the permeability and porosity measurements.

Figure 6.7: Image of CMS-300 permeameter

The results from the permeability tests are provided in Table 6.2. The porosities of the specimens were expected to decrease as the axial load increases before peak stress because of the volumetric contraction observed in Figure 5.3 and Figure 5.4. During loading, the degree of damage is expected to increase and thus enhance the overall permeability of the sample. Our results in Table 6.2 suggest that the porosity trend is consistent with the expectation except for the unstressed specimen, which could be due to sample variations. The specimen that was never loaded using the triaxial device gives the largest permeability, while the specimen loaded to 90% of the peak stress resulted in the lowest permeability. The cause of this unexpected result is discussed next.

Table 6.2: Results from permeability tests

Loading Condition (%)	Confining Pressure (psi)	Pore Volume (cc.)	Porosity (%)	Permeability (md)
0	500	3.027	5.40	8.33E-002
30	500	3.650	6.71	2.05E-002
60	500	4.422	5.60	4.52E-002
90	500	2.839	4.87	1.17E-002

Upon further examination of this sample, there was a large fracture that propagated across the face of the unstressed specimen and through its entire length (Figure 6.8a). There were also small hairline fractures visible on the top face of the specimen. There appeared to be more cracks on the unstressed specimen compared to the loaded ones (Figures 6.8b-d), suggesting that the unstressed specimen inherited some higher initial damage. This allows for a preferential path for gas to pass through the sample and thus results in higher permeability. In addition, we recognized that the unstress sample has never been subjected to the 5 MPa confining pressure which were present in other samples. This could result in a higher connectivity of its pores compared to those loaded

ones, thus contributing to its high permeability. Finally, the 60% loaded sample also exhibit a large fracture passing through the sample (Figure 6.8c). This crack would similarly allow for a preferential path for the gas to travel through, resulting in a higher permeability than the 30% and 90% loaded sample.

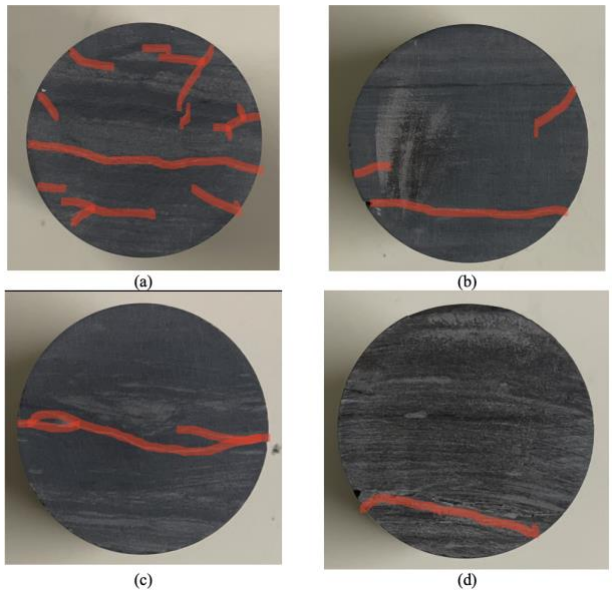

Figure 6.8: Images of cracks present present in samples which were (a) not loaded, (b) loaded to 30% peak stress, (c) loaded to 60% peak stress, and (d) loaded to 90% peak stress

In summary, we believe that the cracks (preexists or induced) in each specimen dominated the permeability results. It is uncertain what are the exact origins of these cracks. Damage could come from the rock formation, initial sampling by the supplier, lab storage, size-reducing cutting at CSM, and sample transportation, although we wish the only source of variation is the % of deviatoric loading on the triaxial device. For future permeability tests, it would be useful to either preload samples that fit the dimensions required by the device or modify the triaxial device to directly measure the permeability during different stages of loading in-situ. The modification of the triaxial device itself would reduce some of the variabilities mentioned above as well as more closely link the level of damage induced by loading to the change in permeability measurement.

CHAPTER 7: CONSTITUTIVE MODELLING OF SHALE

7.1 Introduction

The objective of this chapter is to interpret the triaxial test results on Mancos Shale through a recently developed microcrack directional damage model by Sisodiya (2021), and to conduct Finite element (FE) analysis based on this model to understand the performance of shale as a host rock for deep geological disposal of HLW. Specifically, the constitutive model is calibrated using a MATLAB driver to reflect the experimental results obtained from the three room-temperature high-pressure triaxial tests conducted on Mancos Shale. The calibrated parameters are then taken to an existing user material subroutine (UMAT) which, in conjunction with ABAQUS, to run FE simulation of initial-boundary-value problems. The UMAT is verified by comparing a single element model to the MATLAB results. ABAQUS is then utilized to investigate the long-term deformations that would occur if a tunnel was excavated in a larger shale rock mass.

7.2 Directional Damage Model Basics

The directional microcrack damage model was developed by Sisodiya and Zhang (2021, 2022) and based around the continuous hyperplasticity theory (Houlsby and Puzrin 2007). It captures the evolution of a continuous distribution of microcrack density at different orientations in brittle rocks under compressive loading. The motivation for developing this model was to overcome challenges presented by traditional models which are limited in their ability to represent and track microcrack distributions resulting from complex loading paths (Sisodiya 2021). The model utilizes a damage evolution law which considers initial damage, energy, and resistance to damage to capture the time-dependency behavior of microcrack growth. Below I summarize the basic skeleton of the

model. More details of the theory can be found in Sisodiya and Zhang (2021, 2022) and Sisodiya (2021).

The directional damage, $\hat{d}(\omega)$, is a dimensionless variable that accounts for microcrack effects through a continuum damage mechanics lens. The microcrack-induced directional damage along a given orientation, ω , and expressed by the following equation:

$$\hat{d}(\omega) = \int_0^{a_{max}} \frac{N}{A} a^2 \hat{\rho}(\omega, a) da \tag{7.1}$$

This equation incorporates microcrack distribution density ($\hat{p}(\omega, a)$), the number of microcracks (N), the area of the representative element volume (A), and the half-size of the crack (a).

The directional damage evolution law proposed by Sisodiya and Zhang (2021) is as follows:

$$\dot{\hat{d}} = B \left\langle \frac{\hat{\chi}_d}{\hat{\kappa}} - 1 \right\rangle^{n/2} \tag{7.2}$$

where B is a positive value that controls the rate of damage evolution, $\hat{\kappa}$ represents the material's resistance to damage growth, $\hat{\chi}_d$ represents the energy release rate due to damage growth, and n is a material constant that affects the rate of damage evolution. The Macaulay bracket, $\langle\ \rangle$, is utilized here such that $\langle x \rangle = x$ for $x \geq 0$ and $\langle x \rangle = 0$ for $x < 0$. As a result, the energy release rate must exceed the resistance to damage before damage growth occurs. This value is calculated by the equation:

$$\hat{\chi}_d = 2b\left(\tau' - \hat{\tau}'_f\right)^2 \tag{7.3}$$

where $b = \frac{\pi(k+1)}{16\mu}$ with $k = 3 - 4v$, ν is Poison's ratio, and μ is the shear modulus. As the generated shear stress, τ', exceeds the shear stress required to cause sliding, $\hat{\tau}'_f$, the energy release rate will increase. The direction undergoing damage growth can then expressed by the equation:

$$\theta^d = \{\omega \in [0, \pi] \mid \hat{\chi}_d - \hat{\kappa} > 0\} \tag{7.4}$$

The damage resistance will also adjust depending on the level of damage present within the rock. Initially, $\hat{\kappa}$ increases and the material strengthens as microcracks propagate. At the critical damage value, d_c, failure is initiated and $\hat{\kappa}$ will begin to decrease with additional increases in damage. The hardening law captures this effect in terms of $\hat{\kappa}$ and $\hat{d}$ by Sisodiya and Zhang (2021) as follows:

$$\hat{\kappa} = \begin{cases} \kappa_c - (\kappa_c - \hat{\kappa}_0) * \left(\dfrac{d_c - \hat{d}}{d_c - \hat{d}_0}\right)^2 & for\ \hat{d}(\omega) \leq\ d_c \\ \dfrac{\kappa_c}{1 + r(\hat{d} - d_c)} & for\ \hat{d}(\omega) >\ d_c \end{cases} \tag{7.5}$$

where κ_c is the peak value of $\hat{\kappa}$ achieved when $\hat{d}(\omega) = d_c$, r is a material constant that controls the strain softening behavior, $\hat{d}_0$ is the initial distribution of directional damage, and $\hat{\kappa}_0$ is the initial damage resistance. The mechanics of this hardening law are presented in Figure 7.1.

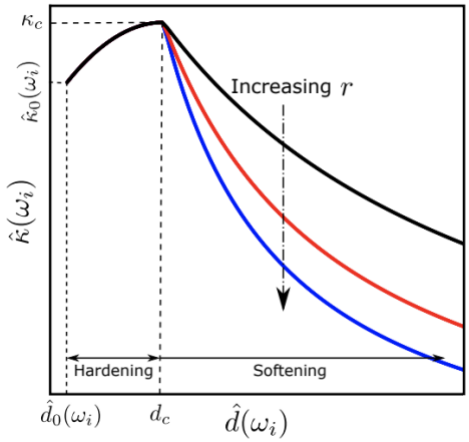

Figure 7.1: Damage hardening law (figure from Sisodiya (2021))

The model considers strain either induced by the opening of microcracks upon frictional sliding, $\hat{\varepsilon}'_D$, or by normal strain induced by crack closure, $\hat{\varepsilon}'_n$. The strain induced by the opening of microcracks is described by the equation:

$$\hat{\varepsilon}'_D = \begin{cases} \frac{\beta}{2}\frac{d|\hat{\gamma}'_f|}{dt} = \frac{\beta}{2} sgn(\hat{\gamma}'_f)\dot{\hat{\gamma}_f}' & for\ \sigma'_{22} \geq 0 \\ 0 & for\ \sigma'_{22} < 0 \end{cases} \tag{7.6}$$

where β is controls the dilative behavior of the material and $\hat{\gamma}'_f$ is the shear strain resulting from sliding along crack faces. The function sgn(·) is the signum function such that sgn(x) = 1 for $x > 0$, sgn(x) = -1 for $x < 0$, and sgn(0) = 0. The sliding induced shear strain can be calculated by:

$$\hat{\gamma}'_f = 4b(\tau' - \hat{\tau}'_f)\hat{d} \tag{7.7}$$

It is important to note that β should be checked to ensure $|\beta| \leq 2\mu_f$ to comply with the second law of thermodynamics, as proved by Sisodiya and Zhang (2021).

The normal strain induced by crack closure is represented by the equation:

$$\hat{\varepsilon}'_n \begin{cases} 0 & for\ \sigma'_{22} \geq \sigma'_c \\ 4b\hat{d}_0\dot{\sigma}'_{22} & for\ \sigma'_{22} < \sigma'_c \end{cases} \tag{7.8}$$

Finally, the peak value of the orientation, ω_p, representing the plane of microcrack coalescence is predicted by the following equation:

$$\omega_p = \frac{\pi}{4} + \frac{tan^{-1}(\mu_f)}{2} \tag{7.9}$$

The equations discussed above were used to construct a constitutive model implemented in a MATLAB package consisting of a driver and a solver. The driver passes the user material input

and user defined load path to the solver, which then solves for the stresses, tangent stiffness, and independent state variables (ISV) given the old state. Six sets of intermediate functions are first calculated by the code as presented in Sisodiya (2021). These intermediate functions calculate compliance and strain tensors and the stiffness and stress tensors are updated by the model. The shear and axial stresses are then defined directly from the updated stress. The internal state functions such as strain rate, $\hat{\kappa}$, $\hat{\chi}_d$, and $\hat{d}(\omega)$ are finally calculated and stored within the model.

7.3 Model Calibration

The current model does not incorporate a temperature dependent component. Therefore, data from the three ambient temperature triaxial tests on Mancos Shale specimens presented in Chapter 5 were used to calibrate the model. The objective during the calibration of the model is to maximumly capture the pressure dependency, dilative behavior, post peak strain softening, and hysteresis resulting from the loading path.

The model contains twelve model parameters including the shear modulus (G), the Poisson's Ratio (ν), the friction angle between crack surfaces (μ_f), the dilation coefficient (β), the stress at crack closure (σ'_0), the reduction rate of $\hat{\kappa}$ (r), the directional damage at failure (d_c), the peak value of damage resistance (κ_c), the base rate of damage evolution (B), the second material constant (n) controlling the rate of damage evolution, the initial isotropic damage (d_0), and the initial damage resistance (κ_0).

The model parameters G, μ_f, ν, σ'_0, and d_0 are first calibrated from the triaxial compression test results. The permanent strains, upon unloading the specimens, are found to be heavily dependent on σ'_0 and d_0. It was determined that σ'_0 must be less than the confining stress, σ'_c, such that the permanent radial and axial strains are plotted and visible at a deviatoric stress of 0 MPa upon unloading. Due to the triaxial machine limitations, data was not obtained during the application of

the confining pressure to interpret how this parameter may affect the radial and axial strains experienced during isotropic compression. Therefore, it is assumed that crack closure occurred at σ'_0 = 5 MPa. It is also observed that increasing the value of d_0 allowed for more permanent strains to occur upon unloading. A value of 1.5 was assigned to d_0 to obtain the closest match to our experimental results. Figure 7.2 demonstrates the effect of d_0 on the resulting permanent strains upon unloading and the stress-strain curvature.

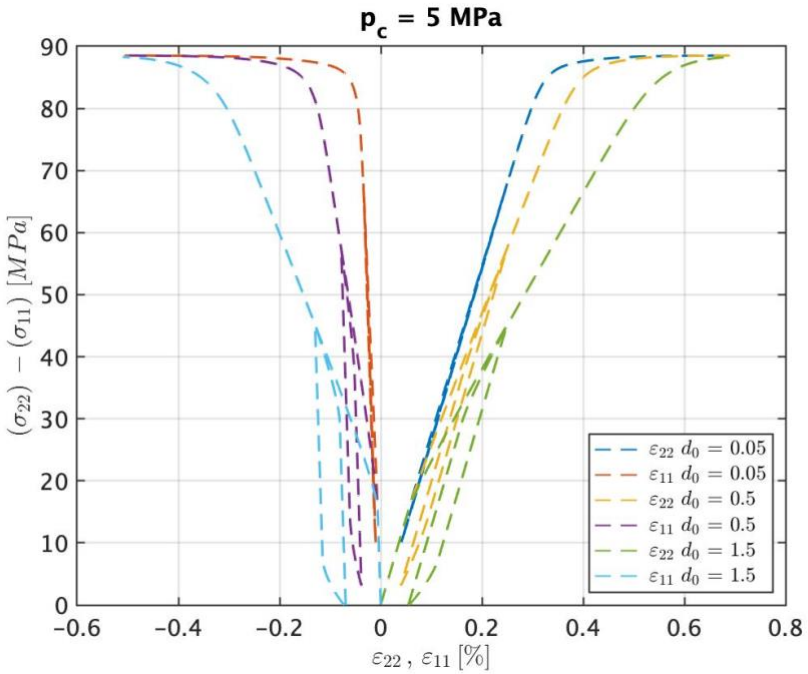

Figure 7.2: Initial damage influence on model predictions

The parameter μ_f primarily controls the peak stress pressure dependency and is set to a value of 0.76. The initial isotropic damage also influences the slopes of the stress-strain curves, and as a result, the shear modulus and Poisson's Ratio are defined as 12.5 GPa and 0.1 respectively to obtain the best-fit slope for both axial and radial strain curves. Increasing μ_f to obtain the necessary pressure dependence causes the peak stresses of tests at all confining pressures to increase. To reduce these peak stresses, κ_c, is reduced such that the onset of failure is initiated earlier, as shown in Figure 7.3. The calibrated κ_c is taken as 7.4 kPa.

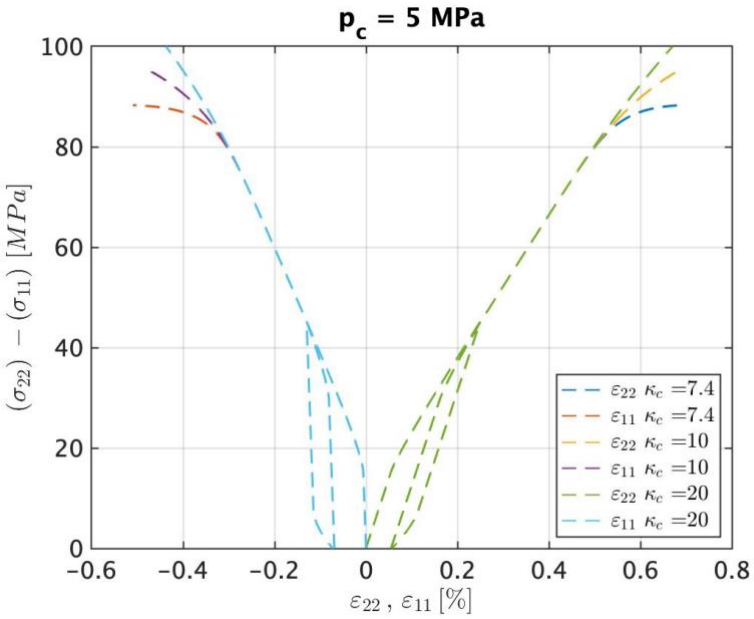

Figure 7.3: κ_c influence on model predictions

The next task is to fit the curve of the stress strain plots to match the experimental data. The main parameters controlling the curvature of the plots are β and κ_0, where κ_0 must be less than κ_c. Increasing κ_0 causes the slope of the stress strain plots to remain more linear until the initial onset of failure which was observed experimentally for axial strain. To obtain the best fit, κ_0 is taken set to 7 kPa. The influence of κ_0 on the model curvature is shown in Figure 7.4.

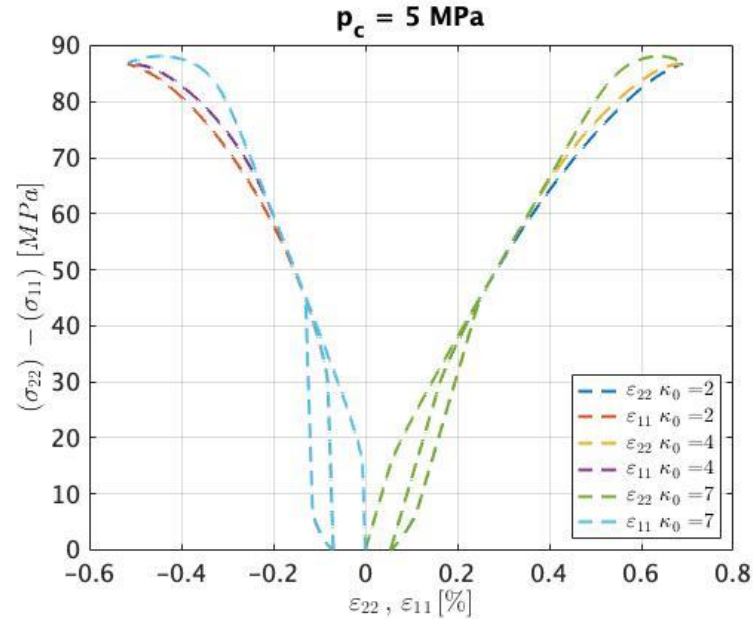

Figure 7.4: κ_0 influence on model predictions

Similarly, β controls the curvature of the stress-radial strain plot, ultimately affecting the dilative response of the material. As β becomes more negative, the material will become more dilative. A schematic of how β affects the stress strain curvature was produced by Sisodiya (2021) and shown below in Figure 7.5. For calibration purposes, β was determined to be -0.2 to best match the materials response based on the experimental data.

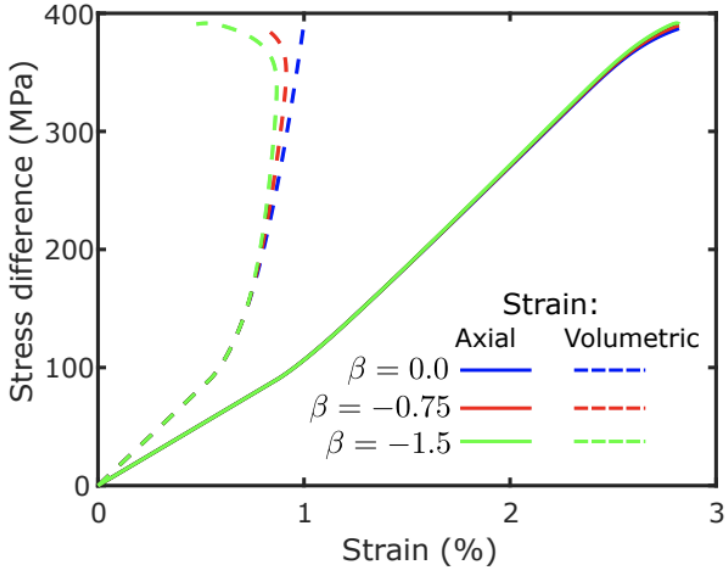

Figure 7.5: Influence of β on dilative behavior (figure from Sisodiya (2021))

To predict the post-peak strain-softening behavior, the parameter r (the reduction rate of $\hat{\kappa}$) is manipulated. Increasing r increases the rate of which $\hat{\kappa}$ reducing the ability to resist damage. This essentially leads the model to predict stronger strain softening behaviors for the material. However, the model becomes much less stable at post-peak strains and presents challenges when implemented in multiple element ABAQUS models. The model is calibrated with r = 0.09 but is later changed to 0.0 for ABAQUS simulations to eliminate convergence issues. Figure 7.6 demonstrates this relationship between r and the strain softening behavior.

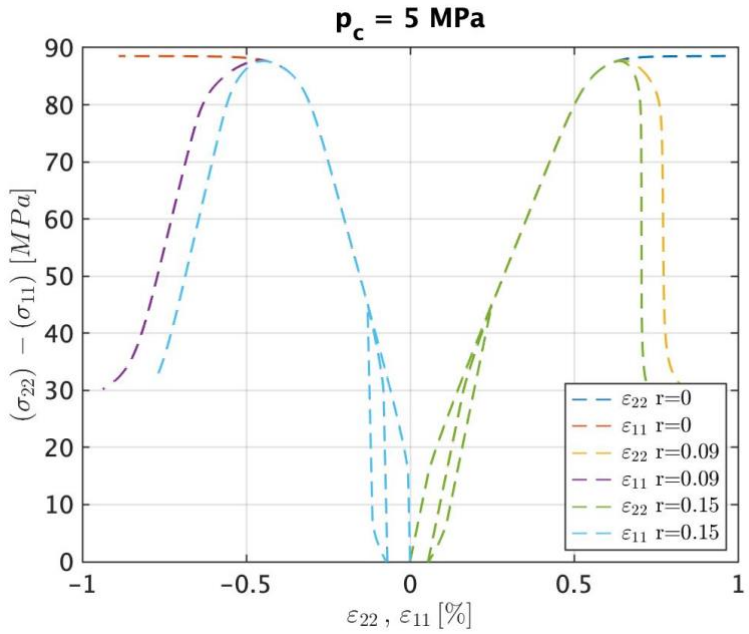

Figure 7.6: Strain softening behavior due to r

The final two parameters that calibrated are *B* and *n* which influence the time rate of damage evolution. To properly calibrate these parameters, creep or relaxation tests are typically required. If creep tests are performed, *B* and *n* can be calibrated by best fitting the creep rate vs. stress difference data. Due to the lack of such experimental data, *B* is set to 4.1667e-7 sec^{-1} and *n* is set to 12 based on previous calibration on Mt. Etna Basalt (Sisodiya and Zhang 2021). A summary of all 12 calibrated parameters is presented in Table 7.1 below.

Table 7.1: Calibrated parameters for directional damage model

Parameter	G	v	μ_f	σ'_c	β	B	n	d_c	κ_c	r	d_0	κ_0
	(GPa)			(MPa)		(sec^{-1})			(KPa)			(KPa)
Value	12.5	0.1	0.76	5.0	-0.2	4.1667e-7	12	2.75	7.4	0.09	1.5	7

These calibrated parameters allowed us to best fit the model to our experimental data. To compare the model predictions to the experimental results, both sets of stress-strain curves are presented in Figures 7.7 – 7.9 for each confining pressure.

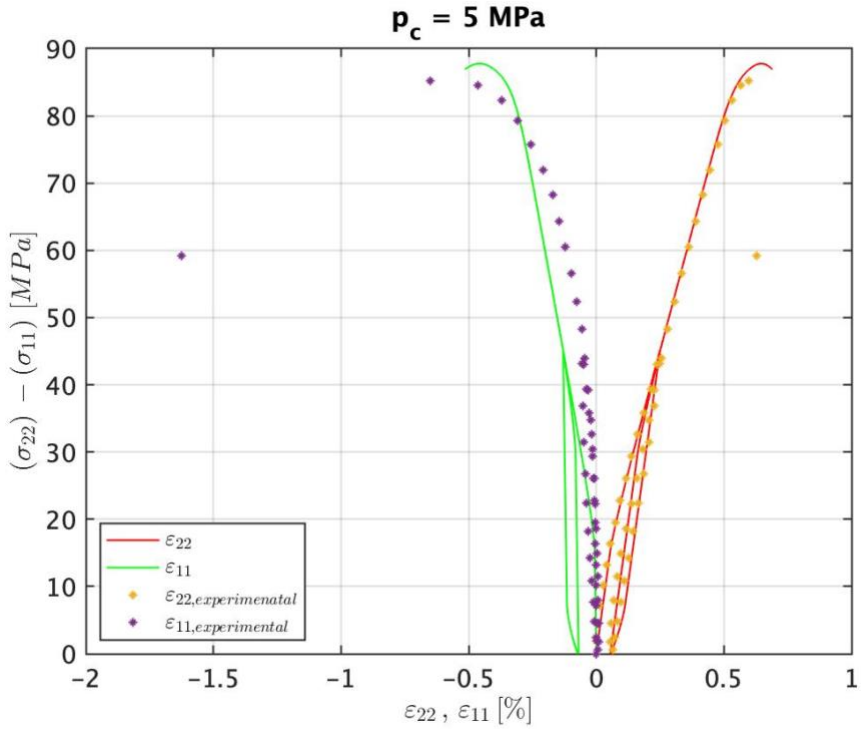

Figure 7.7: Comparison of model prediction and experimental results at under confining pressure of 5 MPa

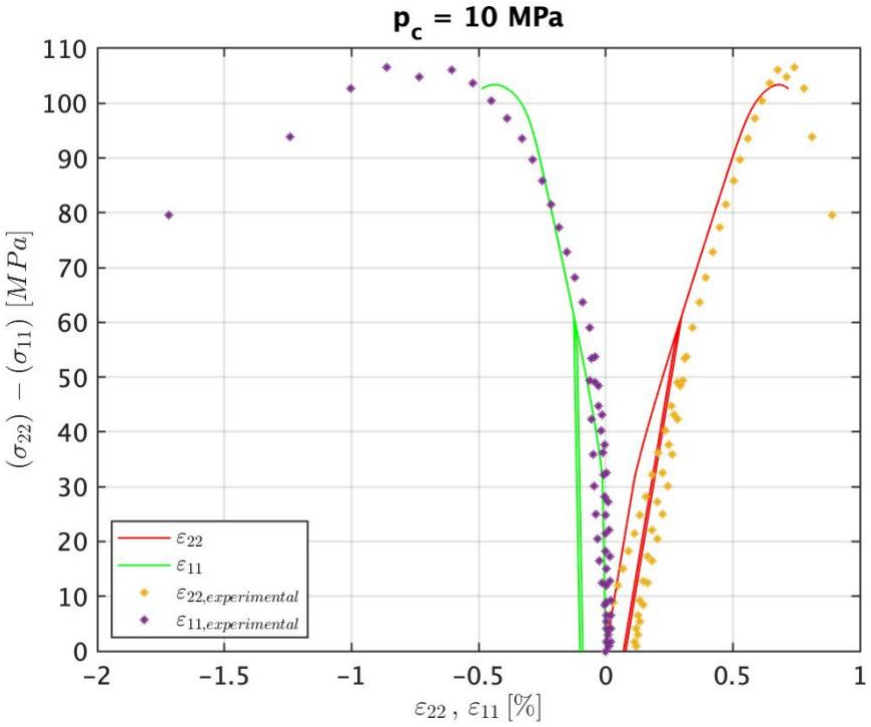

Figure 7.8: Comparison of model prediction and experimental results at under confining pressure of 10 MPa

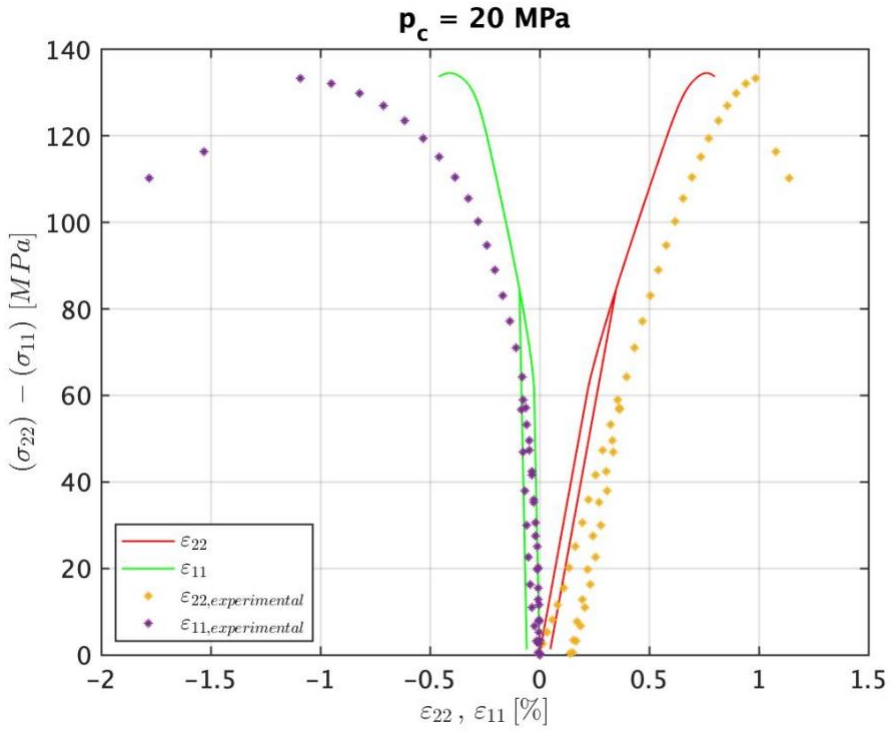

Figure 7.9: Comparison of model prediction and experimental results at under confining pressure of 20 MPa

Overall, the model can represent the experimental data reasonably well. At higher confining pressures, it is observed that the model does not predict the curves as accurately, suggesting that further pressure-dependence parameters may be necessary. Furthermore, it is difficult to model the permanent deformations at low stresses, while also allowing for the model to maintain its pressure-dependence and nonlinearity.

One of the advantages of the model is that it can track the distribution of $\hat{\kappa}$, $\hat{\chi}_d$, and $\hat{d}(\omega)$ to produce polar plots with predictions of the directional damage distribution. The three plots below offer an example of $\hat{\kappa}$, $\hat{\chi}_d$, and $\hat{d}(\omega)$ directional distributions at the end of the triaxial tests. These plots can additionally be used to visualize the orientation of damage in samples. Figure 7.10 - Figure 7.12 demonstrate these three distributions at different strain percentages for tests conducted at 5 MPa.

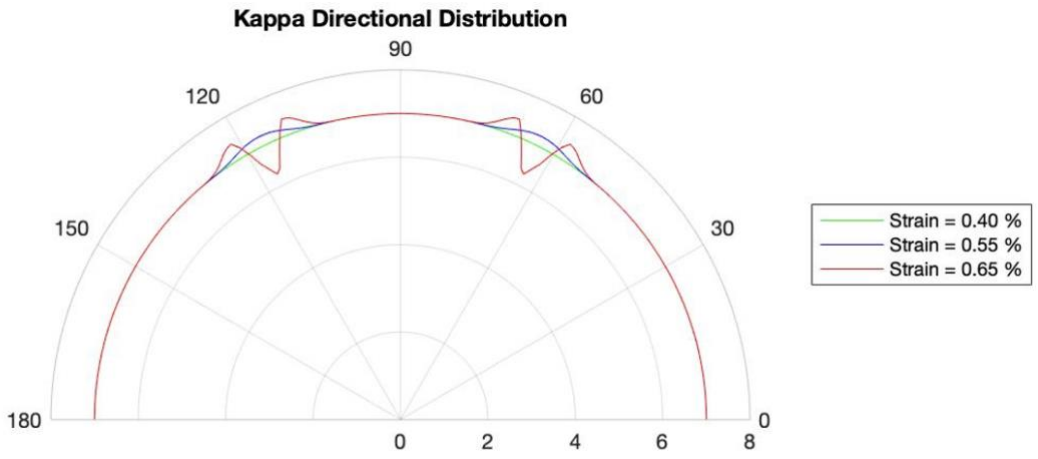

Figure 7.10: Kappa distribution evolution under confining pressure of 5 MPa

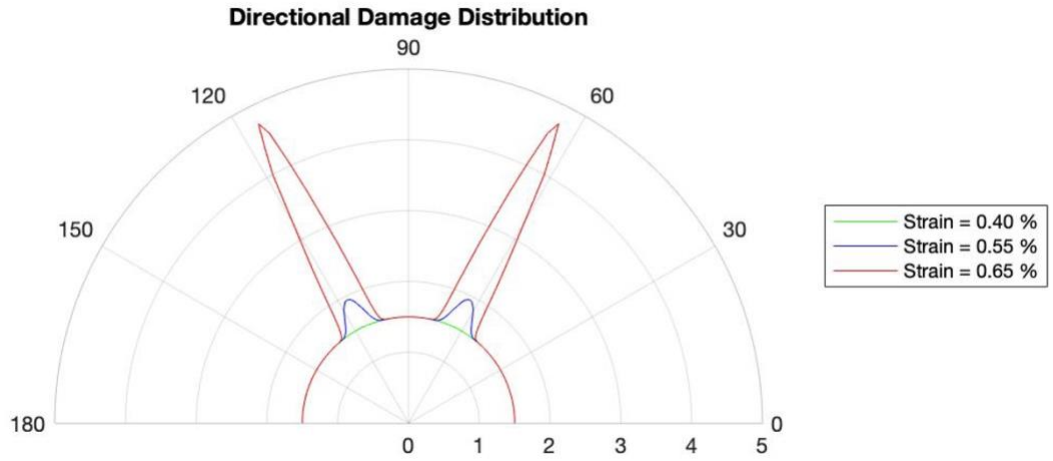

Figure 7.11: Directional damage distribution evolution under confining pressure of 5 MPa

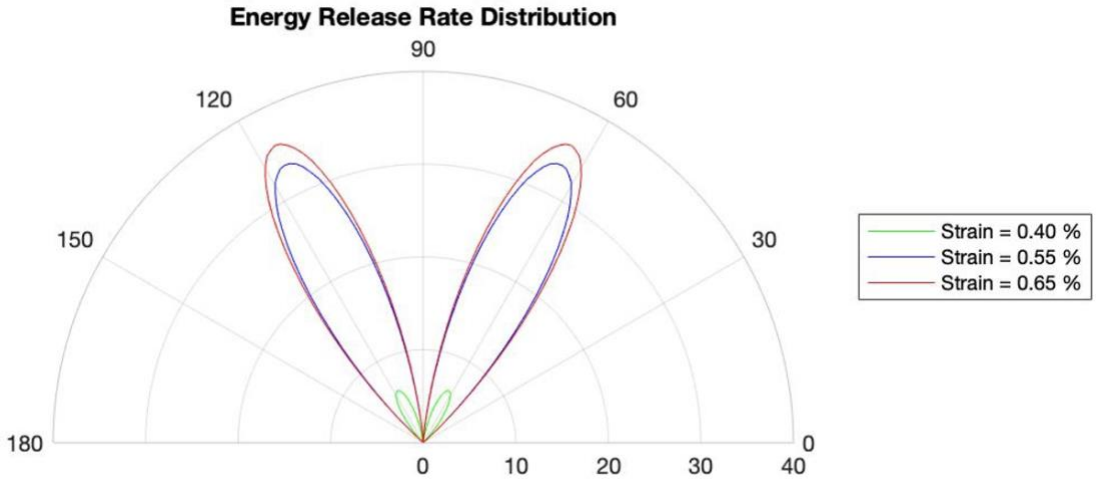

Figure 7.12: Energy release rate distribution evolution under confining pressure of 5 MPa

From the analysis, it was found that there is no change in damage until 0.4% strain is reached due to $\hat{\chi}_d$ being less than the resistance to damage, $\hat{\kappa}$. Essentially this means that the energy experienced by the system is less than that required to initiate crack propagation and strain is only associated with the sliding of crack surfaces. If there is no change in directional damage, there will consequently be no change in $\hat{\kappa}$, as described by Equation 7.5. The distributions of $\hat{\kappa}$ and $\hat{d}(\omega)$ at 0.4 %, 0.55 %, and 0.65 % strain, demonstrate how these distributions evolve after the necessary strain for damage growth is reached. During the consolidation stage up to the point of 0.4 % strain, the distributions are identical. At 0.65 % strain, $\hat{d}(\omega)$ is shown to be greater than d_c at orientations between 58° - 70° and 110°-122° resulting in a decrease in $\hat{\kappa}$ after an initial increase. This represents the material initially experiencing an increase in the resistance to damage during initial damage growth followed by a decrease due to softening.

7.4 ABAQUS single element verification

Once the model was calibrated, an ABAQUS user material subroutine (UMAT) code for the same model is adopted to run large-scale finite element simulations. To verify the model works properly in ABAQUS, elemental tests on a 1m-by-1m square are performed using the same calibrated material parameters and compared to the MATLAB result. It is expected that these two results should be identical.

It's also important to note that the model is implemented as a 2D plane strain problem, which is equivalent to running a plane strain active (PSA) test and results in a stress path different from triaxial tests by maintaining the condition $\varepsilon_2 = 0$. However, very similar material responses are obtained when compared to triaxial test results.

Within ABAQUS, the model geometry is first defined, and the material property is created. 720 solution-dependent variables are used to store the internal variables of the model. All parameters are defined as user materials in the material property except for d_0 and κ_0 which are instead edited within the UMAT code itself. The mesh controls are also assigned to be plane strain in the ABAQUS model to match the UMAT code.

Each test is performed over four steps conducted over 10,000 fixed increments. The element is constrained in the *x*-direction on the far-left side and in the *y*-direction on the bottom during the initial step. During the first step, the confining pressure is applied to the specimen. Steps 2 – 4 are conducted using strain-controlled procedures where the top displacement is defined during each step to load or unload the specimen. The second step loads the specimen to the defined strain that resulted at a stress of about ½ the peak deviatoric stress. Next, the specimen is unloaded in the third step to the strain that produces a deviatoric stress of 0 MPa. The fourth step reloads the specimen to failure. For all steps within this single element model, the axial displacements and times over which the steps occur are identical to the values input into the MATLAB constitutive driver.

Table 7.2 lists the top displacements that are used for steps 2 through 4. The durations over which each step is conducted for each test is also reported in the table. Since all confining pressures are applied rapidly in real experiments, the confining pressure in step 1 is also applied rapidly over 120 seconds with fixed increments of 0.012 s in the simulation.

Table 7.2: Step displacements, time, and increments for loading path

	Step 2 (Initial Loading)	Step 3 (Unloading)	Step 4 (Reloading)
Confining Pressure = 5 MPa			
Top Displacement (m)	-0.0053	-0.0033	-0.0097
Total Time (s)	5325	2000	6400
Increment Size (s)	0.5325	0.2	0.64
Confining Pressure = 10 MPa			
Top Displacement (m)	-0.006	-0.0036	-0.0102
Total Time (s)	6000	2400	6600
Increment Size (s)	0.6	0.24	0.66
Confining Pressure = 20 MPa			
Top Displacement (m)	-0.0068	-0.00375	-0.0118
Total Time (s)	6800	3050	8050
Increment Size (s)	0.68	0.305	0.805

The UMAT code used to implement the ABAQUS model was written following a similar procedure to the MATLAB code; therefore, it is expected that the solutions be exactly the same. During the calibration process, strains experienced during the application of confining pressure are ignored due to lack of experimental data and equipment limitations. In Figures 7.13 – 7.15 below, these strains during confining pressure for both the ABAQUS and MATLAB solutions are compared. Since both these models predict the strains obtained during the application of confining pressure, the curves appear to be shifted to the right compared to the experimental data. For future usage of the model, it would be useful to collect data describing the material response during

confining pressure application. One can see that identical solutions are obtained from the MATLAB and the UMAT runs, confirming the correctness of the UMAT implementation.

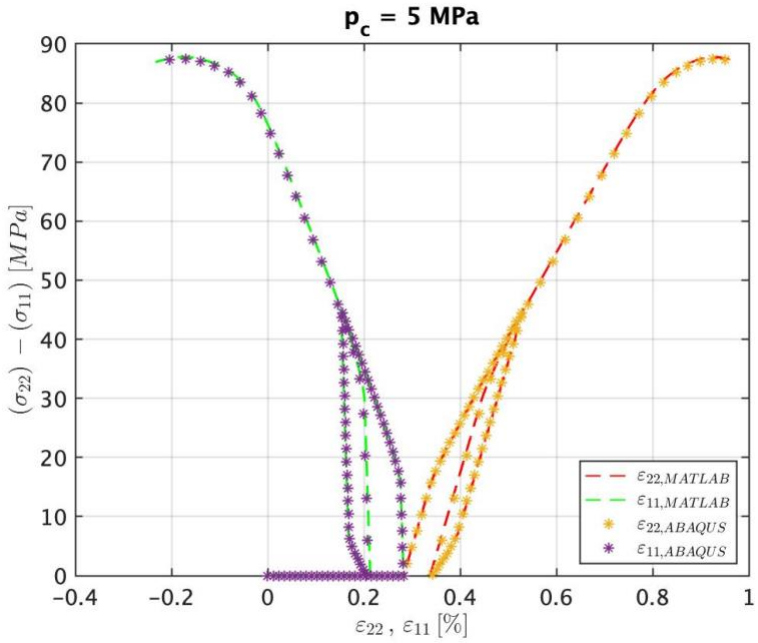

Figure 7.13: Single element ABAQUS solution compared to MATLAB solution at a confining pressure of 5 MPa

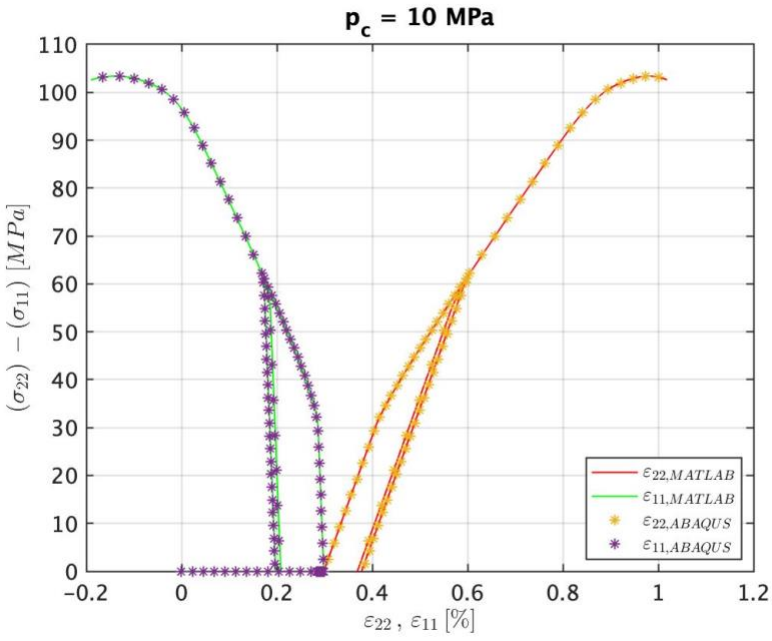

Figure 7.14: Single element ABAQUS solution compared to MATLAB solution at a confining pressure of 10 MPa

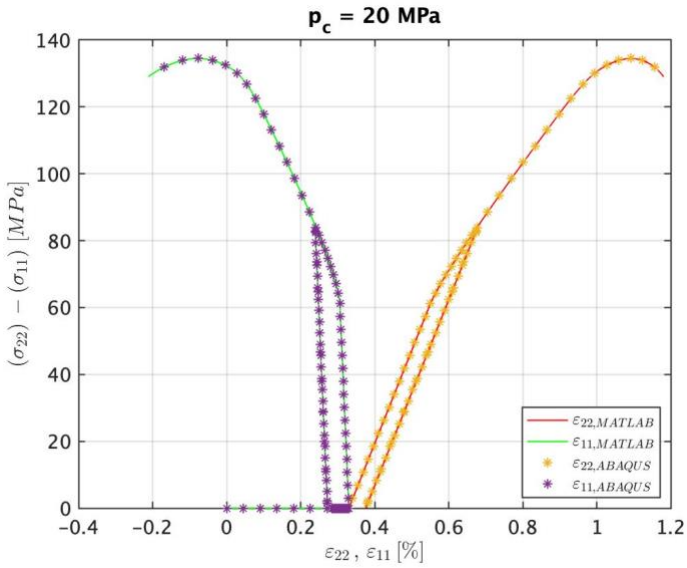

Figure 7.15: Single element ABAQUS solution compared to MATLAB solution at a confining pressure of 20 MPa

7.5 Triaxial Tests in ABAQUS

After checking that the UMAT code worked properly in ABAQUS single element, FE simulations with multiple elements are performed to replicate the triaxial tests performed in the lab. Considering that a plane strain test are conducted in ABAQUS rather than an axisymmetric test, the model is given a geometry that fits the biggest vertical cross-section through the sample such that the entire width and height of the sample was considered.

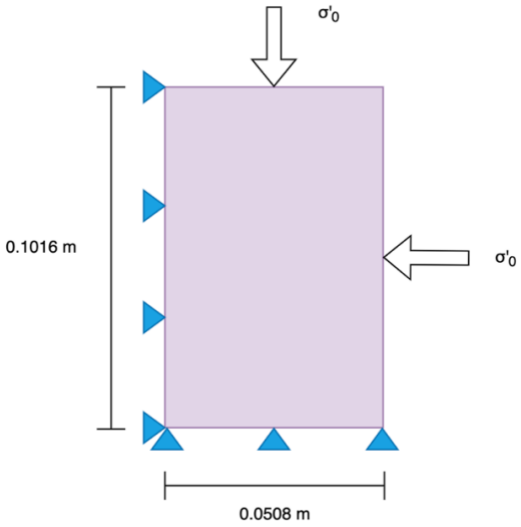

Figure 7.16: Geometry for triaxial tests in ABAQUS

The models is loaded to the same strains with the same time steps as in the single element case, and only the displacements at each step are modified to produce the same strains for the the model geometry. Table 7.3 describes the displacements that were used for the models.

Table 7.3: Step displacements, time, and increment size for load path for adjusted geometry

	Step 2 (Initial Loading)	Step 3 (Unloading)	Step 4 (Reloading)
Confining Pressure = 5 MPa			
Top Displacement (m)	-0.00053848	-0.00033528	-0.00098552
Total Time (s)	5325	2000	6400
Increment Size (s)	0.5325	0.2	0.64
Confining Pressure = 10 MPa			
Top Displacement (m)	-0.0006096	-0.00036576	-0.00103632
Total Time (s)	6000	2400	6600
Increment Size (s)	0.6	0.24	0.66
Confining Pressure = 20 MPa			
Top Displacement (m)	-0.00069088	-0.000381	-0.0119888
Total Time (s)	6800	3050	8050
Increment Size (s)	0.68	0.305	0.805

Analysis is performed almost identically to the single element case, with the main difference being the displacements during the loading path. Another important difference is that the strain softening behavior from the calibrated parameters causes the model to abort when more than two elements are used to mesh the part in ABAQUS. The only parameter affecting the behavior is the parameter *r*. Therefore, this value was set to zero for the multi-element models. This will not have a significant effect on the stress-strain behaviors of the model pre-peak, but it should be recognized

that the model may face challenges when predicting the strain softening behaviors. The model for this analysis was assigned a 60-element mesh with 5 elements horizontally across the specimen by 12 elements down. Figure 7.17 shows the ABAQUS results at each confining pressure plotted together. Overall, the model does a great job at representing the material response observed by the experimental data, with the exception that the strain softening behavior is not captured. The shale material represented by this model is likely too brittle for the model to properly capture the true post-peak behavior.

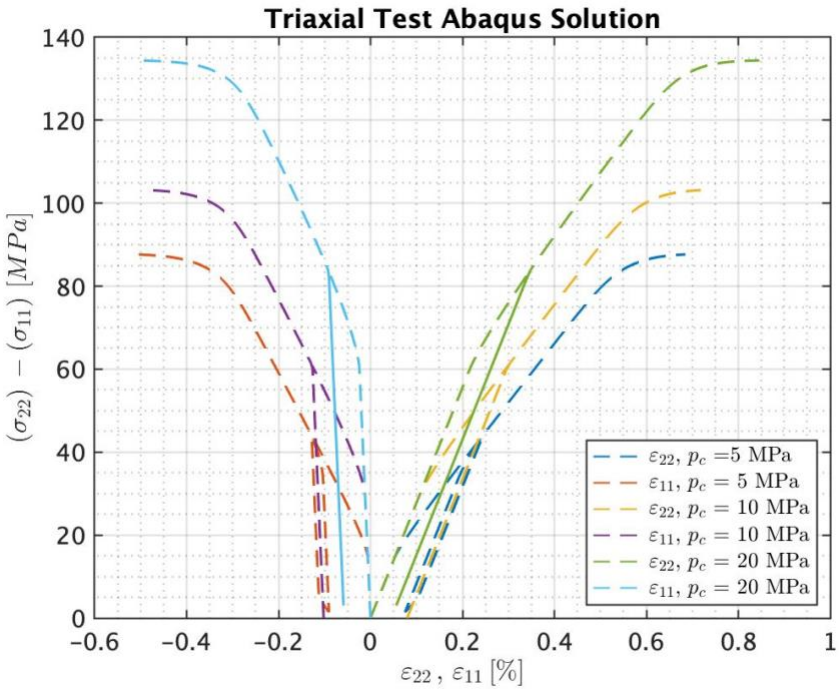

Figure 7.17: Triaxial test simulation implemented in ABAQUS with UMAT code

7.6 Tunnel Problem

The final step for this problem is to analyze how the Mancos Shale will respond 1,000 years after a tunnel is excavated. An in-situ stress of $\sigma'_v = \sigma'_h = 50$ MPa was applied to the model with initial stress distribution was also assumed to be isotropic for simplicity. However, more realistic cases

can be readily studied in future follow-up studies based on this basic model. The geometry for this problem is shown in Figure 7.18.

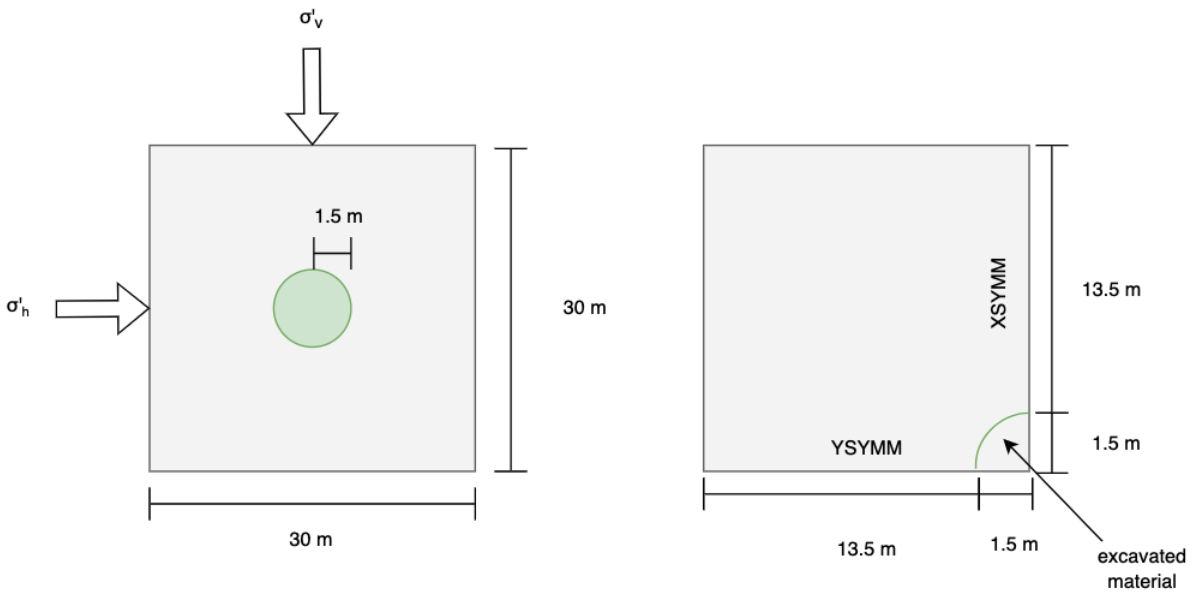

Figure 7.18: Model geometry for tunnel problem

The FE model is created using *y*-symmetry across the bottom face and *x*-symmetry across the right face such that only 1/4th of the total geometry is modeled. The same Mancos Shale parameters used to run the triaxial simulations are used for this simulation as well, with $r = 0$ to remove any potential convergence issues associated with strain softening. The simulation is conducted over 3 steps. The first step allows for geostatic equilibrium where the initial stresses of 50 MPa was installed in the rock mass. The second step simulates the excavation process where the elements corresponding to the excavated rock were deactivated using 'model change'. The excavation was assumed to occur over 1 year duration and the incrementation is done automatically with the smallest increment size being 0.0001 year. The third step allows for creep and stress redistribution after the excavated material is removed. This step is conducted over 1,000 years to observe damage near the tunnel surface. The overall model is meshed by seeding the edges of the excavated zone

with 8 elements. The bottom edge and right-hand edge were seeded to have a total of 22 elements with a bias towards the excavation zone. The top and left-hand boundaries are seeded to have a total 14 elements without any bias.

Figure 7.19 shows the vertical displacements before excavation. Figure 7.20 shows the vertical displacements just after excavation and 1,000 years after excavation. Immediately after excavation, significant amounts of vertical deformations are observed. A slight increase in vertical displacement is observed 1,000 years after the excavation was complete due to creep. The total settlement at the tunnel crown immediately after excavation was predicted to be about 3.2 mm. After 1,000 years, tunnel crown displaced an additional 6.65e-3 mm. This minimum creep effect could be due to the use of the same *B* and *n* value calibrated for the Mt. Etna Basalt which is a much stronger and stiffer rock. The use of realistic *B* and *n* values for shales would have created a much stronger creep settlement overtime. Figure 7.21 show the stress distributions immediately after excavation and 1,000 years after excavation. Again, little stress change is observed during this time, which is expected as the model was ran under mostly stress-controlled conditions.

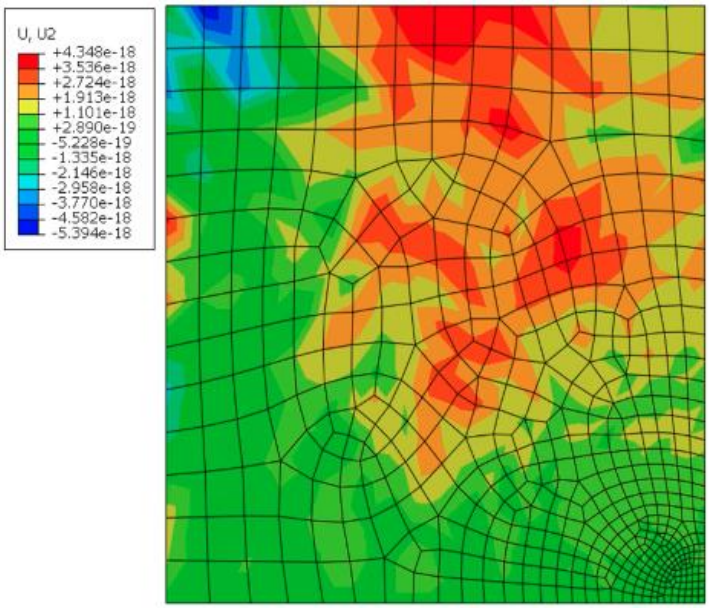

Figure 7.19: Vertical deformations after geostatic equilibrium

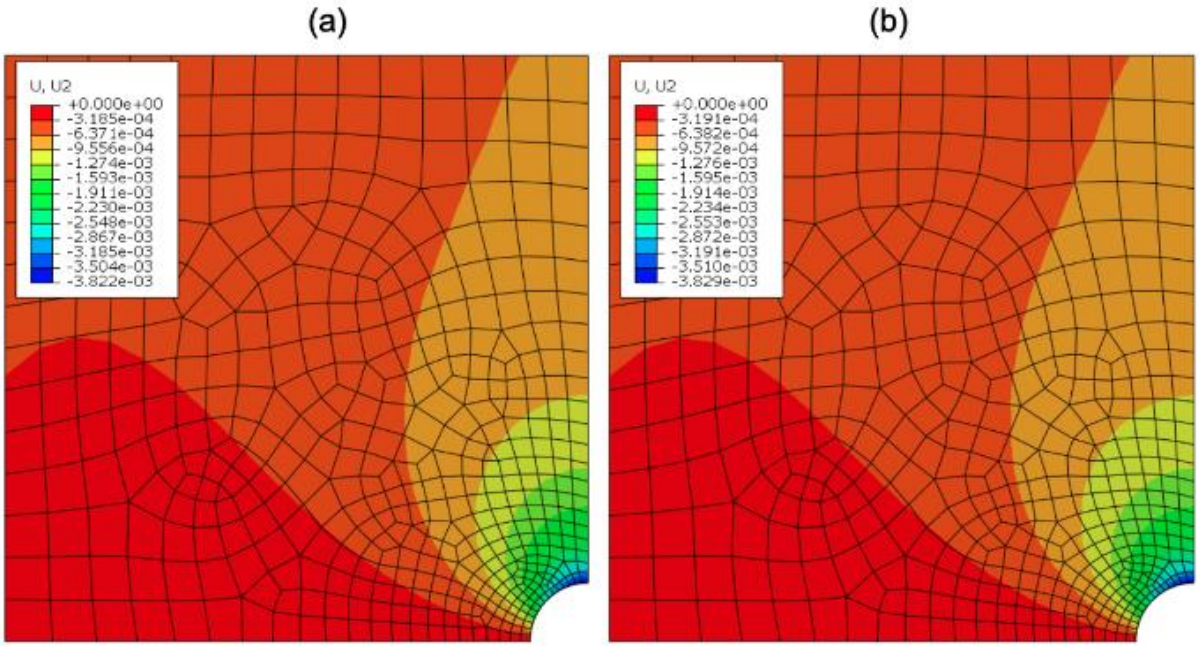

Figure 7.20: Vertical displacements (a) immediately after excavation and (b) 1,000 years after excavation

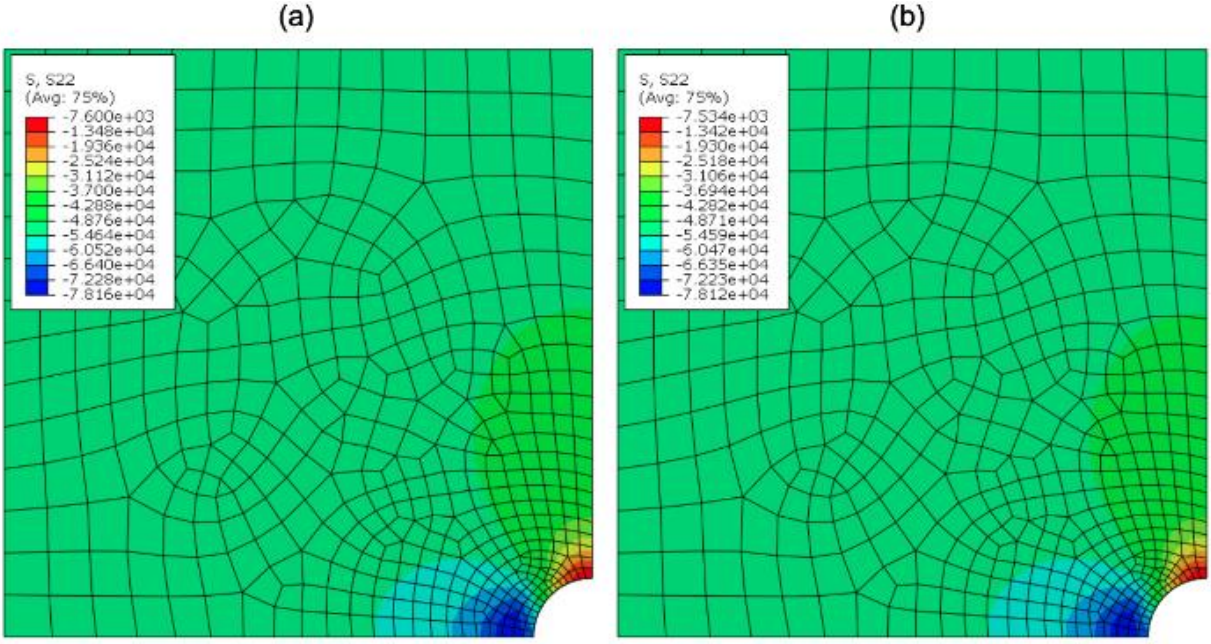

Figure 7.21: Vertical stresses (a) immediately after excavation and (b) 1,000 years after excavation

CHAPTER 8: CONCLUSION

8.1 Conclusions

This thesis outlined the experimental setup and improved procedural method for running high-pressure high-temperature triaxial tests. The improved procedures will pave the way for future triaxial test on mock HEs and other frictional materials at the University of Colorado Boulder. Of most importance is the safety of the operator during experimentation, and precautions to take are thoroughly outlined. The second objective of the improved procedures are to reduce damage to machine components and improve the reliability of test results. Using these methods, an experimental study on the thermo-mechanical behavior Mancos Shale followed by a numerical study was performed and presented in the thesis. The main conclusions are discussed below.

The high-pressure thermal triaxial experiments were performed to study the thermomechanical behavior of shale. The samples used were cut perpendicular to the plane of lamination. The results reveal that the peak deviatoric stresses and Young's Moduli diminished with increasing temperature while the Poison's ratios increased slightly at elevated temperatures. The volumetric strain was observed to be more contractive at larger confining pressures but insensitive to temperature changes. There appeared to be some disagreement in the data trends for tests conducted at 50°C which was likely due to warping of the axial extensometer. Therefore, the numerical study focusses on the ambient temperature results.

Permeability tests were performed to investigate the effect of damage on the permeability of Mancos Shale. The samples used for these tests were cut parallel to the plane of lamination and were loaded to 30%, 60%, and 90% of the peak stress levels at room temperature to obtain different levels of damage. To compare the results, a permeability test was performed on a vertically bedded

specimen that remained unloaded. Due to size limitations of the permeability test apparatus, all samples needed to be cut to reduce the size. The cutting, material variability, and transportation processes likely resulted in additional damage to the samples which was unrelated to the pre-loading process. Upon inspection, the visible cracks were observed on the samples, the density of which are correlated to the permeability results quite well: samples with a greater number of visible cracks had higher permeabilities.

The final element of this thesis presents the numerical study that was performed using a directional damage model. Data from the triaxial tests performed at room temperature were used to calibrate the model. The calibrated model was then implemented in ABAQUS using a working UMAT code. The model was verified by comparing a single element ABAQUS solution to the MATLAB constitutive driver. Lastly, the model was used to simulate the evolution of damage over the duration of 1,000 years after tunnel excavation. Overall, the model was able to capture the dependence of peak deviatoric stress on confining pressure and the strains experienced during unloading. The model was also shown to capture the strain softening behavior at the constitutive level but becomes unstable for multi-element models in ABAQUS. For future use of the model, creep tests would be useful for the calibration of time dependent parameters to fully understand the time-dependent behavior. This data would allow for insight into the evolution of damage at larger time scales.

8.2 Future works

Changes are underway to further improve safety, results, and ease of use when working with the CUBoulder Triaxial device. Specifically, a new user interface for testing has been designed and will be implemented in the future. The interface will remove the manual use of the servo-controller during the test preparation phase. The user should be able to input the desired load values from the

computer and then switch to the control mode of choice. The user will also be able to easily switch between control modes, i.e., switch from force to displacement control without fully unloading the samples. This can be done during test preparation or while tests are being executed. The system continuously reads the voltage values from all sensors regardless of the control mode. If the user wishes to switch from force to displacement control the computer will use the current voltage value from the frame LVDT as the initial value when the mode of control is changed. This system update will further minimize operator error and improve the overall safety of the lab environment. In addition to the new user interface, we plan to connect the system to its own hydraulic pump to prevent test interruption due to other high-pressure systems in the lab which currently operate off the same pump.

Further improvements include reintroducing the ability to apply pore pressure to samples and potentially conducting permeability tests. To allow for pore pressure application, the pore actuator must be fixed to prevent leakages within the system or simple systems such as ISCO pumps can be connected to the apparatus through the pore pressure ports and apply lower pore pressures. Two methodologies could be implemented to improve the permeability results for future testing. 1) The triaxial device at the CUBoulder can be modified to apply pore pressures to the specimens. With this modification, permeability tests could be performed on a single sample at each stage of loading. This would eliminate the need to use cut samples. For samples such as shale, which have low permeabilities and are dissolvable in fluid, gas would need to be used rather than fluid which is possible with the appropriate modifications. When using gas to apply pore pressures or measure permeabilities, an exterior gas tank connected to a regulator can be installed to the apparatus. 2) If modification of the triaxial device for in-situ permeability testing is not feasible in the short term, smaller samples matching the dimensions required for the permeability test apparatus could be

directly used in the triaxial testing phase to eliminate sample cutting process. All other procedures would remain the same as discussed in Chapter 6.

For the numerical simulation, future works are needed on: 1) better calibration of rate-dependent parameters for shale, so that the creep response and the convergence of the tunnel in shale can be more realistically predicted; 2) expand the directional damage model for thermal effect; 3) consider post-closure heating of the tunnel to realistically mimic the permanent storage phase of HLWs.

Future work with this device will ultimately be used to support the work of the PSAAP project which will involve the testing of 1-inch in diameter by 2-inch in heigh mock HE materials. Initial tests will be conducted on F-50 sand samples in binder to provide preliminary data to modelers. For all tests, the thermal triaxial device must be modified to account for the difference in sample size compared to the 2-inch in diameter by 4-inch in diameter shale samples. These samples have much lower compressive strengths and require the addition of a more sensitive load cell which will be calibrated and installed. The plan for these tests is to first conduct simple monotonic tests and high temperature compression tests to compare results to similar works conducted by Yeager (2020). Finally, tests will be performed at various confining pressures at elevated temperatures to further understand the thermomechanical behavior of mock HEs.

REFERENCES

Armand, G., Leveau, F., Nussbaum, C., de La Vaissiere, R., Noiret, A., Jeaggi, D., Landrein, P., Righini, C. 2014. "Geometry and properties of the excavation-induced fractures at the Meuse/Haute-Marne URL drifts." *Rock mechanics and rock engineering* 47(1), 21-41

Berg, H. P., Brennecke, P. 2013. "Management of nuclear-related research and development (R&D)." *Managing Nuclear Projects*, 152-174

Blümling, P., Bernier, F., Lebon, P., Martin, D. C., 2007. "The excavation damaged zone in clay formations time-dependent behaviour and influence on performance assessment." *Physics and Chemistry of the Earth, Parts A/B/C*, 32(8-14), 588-599

Brace, W. F., Walsh, J. B., Frangos, W. T. 1968. "Permeability of granite under high pressure." *Journal of Geophysical research*, 73(6), 2225-2236

Chandler, M. R., Philip, M. G., Brantut, N., Crawford, B. R. 2017. "Effect of temperature on the fracture toughness of anisotropic shale and other rocks." *Geological Society, London, Special Publications*, 454 (1), 295-303

Gao, Q., Tao, J., Hu, J., Yu, B. 2015. "Laboratory study on the mechanical behaviors of an anisotropic shale rock." *Journal of Rock Mechanics and Geotechnical Engineering*, 7(2), 213-219

Geng, Z., Bonnelye, A., Chen, M., Jin, Y., Dick, P., David, C., Fang, X., Schubnel, A. 2016 "Time and temperature dependent creep in Tournemire shale." *Journal of Geophysical Research: Solid Earth*, 123(11), 9658-9675

Grambow, B. 2016. "Geological disposal of radioactive waste in clay." *Elements*, 12(4), 239-245

Gratton, M., Gontier, C., Allah, S.R.F., Bouchou, A., Picart, D. 2009. "Mechanical characterisation of a viscoplastic material sensitive to hydrostatic pressure." *European Journal of Mechanics-A/Solids*, 28(5), 935-947

Huang, S. L., Aughenbaugh, N. B., Rockaway, J. D. 1986. "Swelling pressure studies of shales." *International Journal of Rock Mechanics and Mining Sciences & Geomechanics Abstracts*, 23(5), 371-377

Herman, M. J., Woznick, C. S., Scott, S. J., Tisdale, J. T., Yeager, J. D., Duque, A. L. 2021."Composite binder, processing, and particle size effects on mechanical properties of non-hazardous high explosive surrogates." *Powder Technology*, 391, 442-449

Houlsby, G.T., Puzrin, A.M., 2007. *Principles of hyperplasticity: an approach to plasticity theory based on thermodynamic principles*. Springer Science & Business Media.

Islam, A. Md., Skalle, P. 2013. "An experimental investigation of shale mechanical properties through drained and undrained test mechanisms." *Rock Mechanics and Rock Engineering*, 46(6), 1391-1413

Josh, M., Esteban, L., Piane, D. C., Sarout, J., Dewhurst, D. N., Clennel, M. B. 2012. "Laboratory characterisation of shale properties." *Journal of Petroleum Science and Engineering*, 88, 107-124

Kang, Y., Chen, M., You, L., Li, X. 2015. "Laboratory measurement and interpretation of the changes of physical properties after heat treatment in tight porous media." *Journal of Chemistry*, 2015

Karman, T. 1911. "Tests on Materials under Triaxial compression." *Verein Deutscher Ingenieure (Berlin)*, 42

Kim, J. S., Kwon, S. K., Sanchez, M., Cho, G. C. 2011. "Geological storage of high level nuclear waste." *KSCE Journal of Civil Engineering*, 15(4), 721-737

Kwon, O., Kronenberg, A. K., Gangi, A. F., Johnson, B., Herbert, B. E. 2004. "Permeability of illite-bearing shale: 1. Anisotropy and effects of clay content and loading." *Journal of Geophysical Research: Solid Earth*, 109(B10)

Lora, R. V., Ghazanfari, E., Izquierdo, E. A. 2016. "Geomechanical characterization of Marcellus shale." *Rock Mechanics and Rock Engineering*, 49(9), 3403-3424

Lu, Y., Wang, L., Sun, X., Wang, J. 2017. "Experimental Study of the influence of water and temperature on the mechanical behavior of mudstone and sandstone." *Bulletin of Engineering Geology and the Environment*, 76**,** 645–660

Masri, M., Sibai, M., Shao, J. F., Mainguy, M. 2014. "Experimental investigation of the effect of temperature on the mechanical behavior of Tournemire shale." *International Journal of Rock Mechanics and Mining Sciences*, 70, 185-191

Paterson, M. S., Wong, T. F. 2005. *Experimental rock deformation-the brittle field*. Springer Science & Business Media.

Peterson, P. D., Idar, D. J. 2005. "Microstructural differences between virgin and recycled lots of PBX 9502." *Propellants, Explosives, Pyrotechnics: An International Journal Dealing with Scientific and Technological Aspects of Energetic Materials*, 30(2), 88-94

Sayers, C. M. 2013. "The effect of anisotropy on the Young's moduli and Poisson's ratios of shales." *Geophysical Prospecting*, 61(2), 416-426

Sellin, P., Leupin, O. X. 2013. "The use of clay as an engineered barrier in radioactive-waste management–a review." *Clays and Clay Minerals*, 61(6), 477-498

Sisodiya, M., Zhang Y. 2021. “A time-dependent directional damage theory for brittle rocks considering the kinetics of microcrack growth.” *Rock Mechanics and Rock Engineering*, 55 (5), 2693-2710

Sisodiya, M., Zhang, Y. 2022. “A directional microcrack damage theory for brittle solids based on continuous hyperplasticity”. *International Journal of Damage Mechanics*, published online, DOI: /10.1177/10567895221095890

Sisodiya, M. 2021. “Continuum Damage Mechanics based on Directional Distribution” Doctoral Thesis. University of Colorado Boulder

Tsang, C. F., Bernier, F., Davies, C. 2005. "Geohydromechanical processes in the Excavation Damaged Zone in crystalline rock, rock salt, and indurated and plastic clays—in the context of radioactive waste disposal." *International Journal of Rock Mechanics and Mining*, *Sciences* 42(1), 109-125

United States Nuclear Regulatory Commission. Nuclear Regulatory Legislation. 2013. NUREG-0980. 1(10)

Wang, Y., Porter, D. L., Naleway, S. E., Newell, P. 2021. "Thermo-mechanical characterization of shale using nanoindentation." *Scientific Reports*, 11(1), 1-12

Wang, M., Zang, D. 2021 "Triaxial testing on water permeability evolution of fractured shale." *Royal Society open science*, 8(12), 211270

Yeager, J. D., Woznick, C. S., Thompson, D. G., Duque, A. L., Liu, C., Burch, A. C., Bowden, P. R., Shorty, M., Bahr, D. F. 2020. “Development of a new density and mechanical mock for HMX”. No. LA-UR-18-25764. Los Alamos National Lab. (LANL), Los Alamos, NM (United States)

Zhang, C. L. 2018. "Thermo-hydro-mechanical behavior of clay rock for deep geological disposal of high-level radioactive waste." *Journal of Rock Mechanics and Geotechnical Engineering*, 10(5), 992-1008